Jinst

Published by IOP Publishing for Sissa Medialab

Received: *November 4, 2021*
Revised: *December 21, 2021*
Accepted: *December 27, 2021*
Published: *January 20, 2022*

Comparison of measurement and simulation of ATLAS cavern radiation background

E. Heijne,[g,c] **T. Koi,**[d] **C. Leroy,**[f] **H. Oberlack,**[b] **S. Pospisil,**[c] **P. Sherwood,**[e] **M. Shupe,**[h] **J. Solc,**[c,1,*] **M. Suk,**[c] **H. Takai,**[a] **D. Turecek,**[c,2] **Z. Vykydal**[c,1] **and Ch. Young**[d]

[a] *Brookhaven National Laboratory, Upton, NY, United States*
[b] *Max-Planck-Institut für Physik, München, Germany*
[c] *Institute of Experimental and Applied Physics, Czech Technical University in Prague, Praha, Czech Republic*
[d] *SLAC National Accelerator Laboratory, Menlo Park, CA, United States*
[e] *University College London, London, United Kingdom*
[f] *Département de Physique, Université de Montréal, Montréal (Québec), H3C 3J7, Canada*
[g] *CERN, Geneva, Switzerland*
[h] *Department of Physics, University of Arizona, Tucson, AZ, United States*

E-mail: jsolc@cmi.cz

Abstract: Sixteen Medipix2 pixel detector based (MPX) devices were operated at various positions within the ATLAS detector and cavern continuously from early 2008 up to 2013. In addition to photons, each MPX detector is capable to detect charged particles, and neutrons as it is covered with a mask of converter materials dividing its area into regions sensitive to thermal or fast neutrons. The MPX detector network was effectively used for real-time measurements of the spectral characteristics and composition of complex radiation fields in ATLAS. This article reports comparison of the results of measurements performed with MPX detectors during the LHC operation period in 2010 and 2011 with Monte Carlo simulations results from the FLUGG and GCALOR codes. For the purpose of this comparison, the MPX detectors were operated in tracking mode with low threshold (8–10 keV)

[1] Currently affiliated with Czech Metrology Institute, Brno, Czech Republic.
[2] Currently affiliated with Pure Storage, Praha, Czech Republic.
[*] Corresponding author.

https://doi.org/10.1088/1748-0221/17/01/P01027

2022 JINST 17 P01027

allowing one to distinguish among particle categories based on the recognition of track patterns left by the particles in the MPX sensitive layer. The comparison of measurements with simulations shows that the agreement between measured and simulated data is satisfactory in most cases within a factor of two.

KEYWORDS: Detector modelling and simulations I (interaction of radiation with matter, interaction of photons with matter, interaction of hadrons with matter, etc); Gamma detectors (scintillators, CZT, HPGe, HgI etc); Models and simulations; Particle tracking detectors (Solid-state detectors)

2022 JINST 17 P01027

Contents

1 Introduction **2**

2 Materials and methods **3**
2.1 MPX detectors 3
2.1.1 Brief description 3
2.1.2 Location of MPX detectors in ATLAS 3
2.1.3 Operational parameters 3
2.1.4 Calibration 5
2.2 Characterization of the measured data 5
2.2.1 Definition of quantities 5
2.2.2 Particle tracks pattern recognition 6
2.2.3 Classification of clusters 6
2.2.4 Particle categories 6
2.3 Simulation of the cavern radiation field by FLUGG 7
2.3.1 The model 7
2.3.2 Simulation sample 9
2.3.3 Particle types 9
2.3.4 Neutron spectral fluence distributions 9
2.4 Simulation of the cavern radiation field by GCALOR 10
2.4.1 Particle types 11
2.5 Simulation of the MPX device response by MCNPX 11
2.5.1 The MPX device model 12
2.5.2 Validation 12

3 Results **14**
3.1 Simulation data used for the comparison 14
3.2 Measurement data used for the comparison 16
3.2.1 Correction for overlapping tracks 16
3.3 Thermal neutrons 18
3.3.1 Simulation data 18
3.3.2 Measurement data 18
3.3.3 Comparison of measurement and simulation 19
3.4 Low energy transfer particles 22
3.4.1 Simulation data 22
3.4.2 Measurement data 22
3.4.3 Comparison of measurement and simulation 24
3.4.4 Sensitivity to energy cuts 24
3.5 High energy transfer particles 26
3.5.1 Simulation data 26
3.5.2 Measurement data 27
3.5.3 Comparison of measurement and simulation 28
3.5.4 Sensitivity to energy cuts 30

4 Conclusions **31**

2022 JINST 17 P01027

1 Introduction

The on-detector instrumentation in high energy physics experiments is exposed to a radiation background that originates from the interaction of thousands of particles produced in each collision with the detector material. The electronics components that service the instrumentation can be damaged by the ionizing radiation or susceptible to single event effects leading to data loss or corruption. Thus, the knowledge of the radiation field composition and intensity is critical for the reliable operation of present-day experiments, and has significant impact on the design of upgraded or newly planned colliders [1–5].

The ATLAS detector, now in operation for over 20 years, has introduced a real time radiation field monitoring system that is based on the imaging Medipix device. Implemented in strategic places in the detector, the monitoring devices give a fast turnaround on characterizing the radiation background. Along the years, the results obtained by this system helped the design and implementation of electronics by providing the needed electronics qualification data.

A network of pixel detectors (MPX) based on the Medipix2 chip, which has been developed at CERN in the framework of the Medipix Collaboration [6], was installed within the ATLAS experiment at CERN. It was operated from 2008 to 2013 until the Large Hadron Collider (LHC) was shutdown for an upgrade. It provided real-time information on the radiation field composition within the ATLAS experiment and its environment, including the information on thermal neutrons. The MPX network also measured the induced radioactivity and the associated photon ambient dose equivalent rate in ATLAS [7] and the penetration of ionizing radiation into the service cavern USA15 separated from the main cavern by a 2.0 m thick concrete wall [8].

This paper reports on the methods and results obtained as well as a comparison of measurements with two independent Monte Carlo simulation results, FLUGG and GCALOR. This study was performed for data obtained during the LHC operations in 2010 and 2011. The comparison with the GCALOR simulation package has been already presented by the authors in [5]. Therefore, the paper focuses mainly on the FLUGG simulation results while only a summary of information is presented for GCALOR. Although the idea of this comparison may seem simple, the comparison process is not straightforward. MPX detectors do not distinguish particle types, except for neutrons with help of converters, nor record the deposited energy. Instead, the devices are able to distinguish particle categories based on the pattern recognition of tracks generated by the ionizing radiation quanta in the sensor. The separation between these particle categories is not sharp which invokes an extensive discussion about the proper energy, incidence angle and particle cuts applied on simulation data. For this reason, a detailed model of the MPX device was developed to understand the response of both FLUGG and GCALOR results. The simulation tool is general and could be of interest to a wider community [9].

This paper is organized into several sections. After the Introduction, a short description of the MPX detector features and capabilities together with technique of particle recognition are presented in sections 2.1 and 2.2. Sections 2.3–2.5 is devoted to model the description of the cavern radiation background simulation by FLUGG and GCALOR and to the translation of these simulation results into simulated events expected to be registered in the sensor of a MPX detector at its given location. Section 3 is dedicated to detailed comparison of measurements and simulations. Special attention is paid to the assignment of observed tracks in the sensor to different locally incident particles according to the simulation for the various particle categories.

2022 JINST 17 P01027

2 Materials and methods

2.1 MPX detectors

This section is presenting a description of the MPX detector including its features and capabilities to identify/differentiate among particles. The detector locations in the ATLAS detector environment are given in the section in ATLAS coordinate system.

2.1.1 Brief description

The MPX device consists of a 300 µm thick silicon sensor matrix of 256×256 cells bump-bonded to a pixelated read-out Medipix2 chip. Each matrix element ($55 \times 55\,\mu m^2$) is connected to its respective read-out chain integrated on the read-out chip. The MPX detector has also the capability of measuring neutron fields. Figure 1 shows the mask of converter materials covering the detector and dividing its area into regions sensitive to different types of neutrons (LiF enriched to 89% ^{6}Li and polyethylene for thermal and fast neutrons, respectively) and aluminium layers to filter the radiation field [5]. The MPX detector is used either in counting or in tracking mode for the measurement of the radiation field and its spectral composition within the ATLAS detector [5].

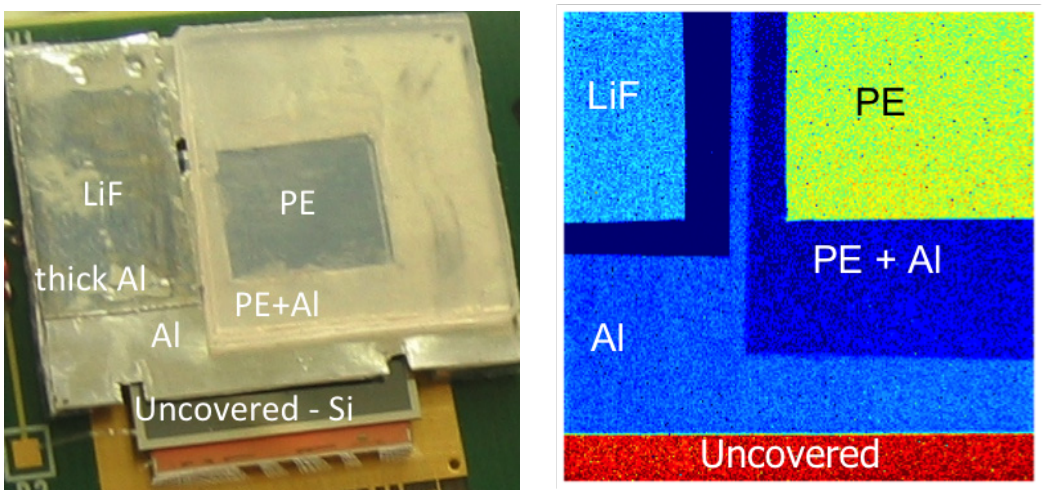

Figure 1. Left — view of a MPX sensor covered with neutron conversion layers and aluminium filters. Right — X-ray image of the conversion layers position above the MPX sensor.

2.1.2 Location of MPX detectors in ATLAS

There were sixteen MPX detectors installed in ATLAS as illustrated in figure 2. Their coordinates are detailed in table 1. MPX01 through MPX15 are considered in this article as the MPX16 was located in the service cavern USA15 outside the geometry used in FLUGG and GCALOR ATLAS simulations.

2.1.3 Operational parameters

For the purpose of comparing results from FLUGG and GCALOR simulations with MPX measurements of the ATLAS radiation field, the devices were operated in tracking mode with low threshold

2022 JINST 17 P01027

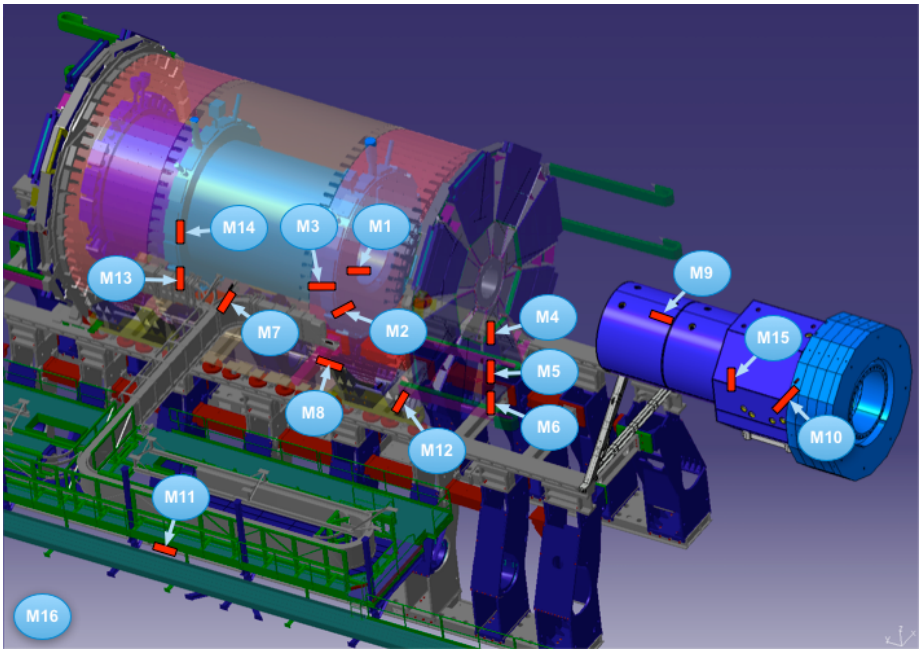

Figure 2. Location of the MPX detectors in ATLAS. "M" in the labels serves as an abbreviation for "MPX".

Table 1. MPX detector locations and positions with respect to the central interaction point. X, Y and Z axes correspond to the standard ATLAS coordinate system, $R = (X^2 + Y^2)^{1/2}$ is the distance from the beam axis at position Z. Approximate orientation of the devices is given with respect to the beam axis (Z axis). Publications [10] and [11] describe the mentioned ATLAS sections.

Name	Location description	X [m]	Y [m]	Z [m]	R [m]	Orientation
MPX01	between ID and JM plug	−0.71	0.29	3.42	0.77	90°
MPX02	between TILE and EB	−2.23	−1.12	3.42	2.50	90°
MPX03	between TILE and EB	−3.45	0.93	2.94	3.57	90°
MPX04	on the Small Wheel	−0.65	−1.30	7.12	1.30	90°
MPX05	on the Small Wheel	−0.55	−2.36	7.20	2.36	90°
MPX06	on the Small Wheel	−0.65	−3.36	7.20	3.36	90°
MPX07	top of TILECAL barrel	−4.53	0.79	0.35	4.59	90°
MPX08	top of TILECAL EB	−4.37	−0.53	4.02	4.40	0°
MPX09	on the JF cylinder	0.00	1.56	15.39	1.56	0°
MPX10	cavern wall HO	−3.96	3.36	22.88	5.19	45°
MPX11	cavern wall USA side	−16.69	0.05	4.86	16.69	0°
MPX12	on the EIL 4	−6.25	0.00	7.23	6.25	90°
MPX13	between TILE and EB, C	−2.21	−1.02	−3.42	2.44	90°
MPX14	between ID and JM plug, C	−0.71	−0.30	−3.43	0.77	90°
MPX15	at the back of LUCID	0.19	−0.08	18.74	0.20	90°
MPX16	USA15	−39.48	0.90	−6.55	39.48	N/A

(8–10 keV). This means that the acquisition time of MPX detector was set short enough in order to distinguish the recorded tracks created by the individual particle interactions.

2022 JINST 17 P01027

Each MPX device was read out as a 256×256 pixels frame with the radiation created events collected after a remotely settable integration time window (frame). Time length of the window was adjusted according to a particle fluence rate at the detector location which is correlated to the distance of the device from the interaction point and beam axis. It ranged from 100 µs for MPX15 during collisions up to 10 min during radiation background measurement outside collisions periods [5].

2.1.4 Calibration

The MPX response to photons and charged particles is consistent from detector to detector. However, the response to thermal and fast neutrons varies due to the technology of converter layer production. Therefore, the response of every MPX device to thermal neutrons has been calibrated in a reference isotropic thermal neutron field, and the response to fast neutrons has been calibrated using ^{241}AmBe and ^{252}Cf sources. The detector-specific detection efficiency for thermal and fast neutrons was accounted for in the evaluation of measured data by the ATLAS-MPX network. The typical detection efficiencies for 300 µm thick Si sensor equipped with neutron conversion layers as shown in figure 1 are as follows:

- About 1% for thermal neutrons (with ^{6}LiF converter);
- About 0.1% for fast neutrons of energy in the range of 1–15 MeV (with PE converter);
- 100% for charged particles with energies above 8 keV;
- About 90% for 10 keV X-rays, 2% for 60 keV X-rays, 0.5% for 662 keV gamma rays; 0.1% for gamma rays with energy above 1 MeV;
- For MIPs the detection efficiency is 100%. However, their recognition depends on the number of the hit pixels in the line, which is determined by the incidence angle of the incoming MIP.

These values determined from calibration measurements were supplemented by detection efficiencies calculated by MCNPX™ [12] for the MPX sensor mounted in the real device (box). The simulated detection efficiencies were used to recalculate the FLUGG and GCALOR results into quantities comparable with MPX measurements (see section 3.1 and [5]). Validation of an MCNPX™ model of an MPX detector is described in section 2.5.2.

2.2 Characterization of the measured data

2.2.1 Definition of quantities

For the purpose of this article, we use the following terminology:

- **Cluster rate**: number of clusters per unit time and unit area. It is equivalent to the quantity "particle current" as described in detail in appendix II in [4];
- **Cluster count**: integrated cluster rate over given integration time period. The integration period can be, for example, exposition time of one frame or time of integration of a luminosity rate to the given value of integrated luminosity;
- **Particle flux**: rate of particles per unit area and unit time independent on particle direction [4];

2022 JINST 17 P01027

- **Particle fluence**: integrated particle flux over given integration time period. In this article we use this quantity to express the thermal neutron fluence per unit integrated luminosity.

2.2.2 Particle tracks pattern recognition

The signature of particles interacting in the silicon layer is seen as a cluster of adjoining activated pixels with different size and shape depending on the type of particles, their energies, incidence angles and the nature of their interactions in the detector sensitive volume. Data collected in the tracking mode were analysed with a pattern recognition algorithm according to their characteristics like:

- area (number of adjacent activated pixels);
- roundness (comparing cluster area to length of its border);
- linearity (consistency of activated pixels in the cluster with straight-line track);
- width of straight track.

These characteristics were stored in a database for each individual particle generated cluster in the frame. The track pattern recognition becomes complicated at high count rates due to the overlapping of tracks. For details, see [5].

2.2.3 Classification of clusters

The clusters analysed with the pattern recognition algorithm were sorted according to the values of the analysed characteristics into six cluster categories corresponding roughly to the types of interacting particles (see figure 3):

1. **Dot** — low energy X-rays and electrons (typical energy 10 keV);
2. **Small blob** — more energetic photons and electrons (typical energy 20–80 keV);
3. **Curly track** — energetic photons and electrons (typical energy hundreds of keV, MeV);
4. **Heavy blob** — energetic particles with low range (alpha particles, ions, etc);
5. **Heavy track** — energetic highly ionizing particles;
6. **Straight track** — relativistic ionising particles (energetic protons, charged pions, muons, MIPs, etc.).

2.2.4 Particle categories

For the purpose of the comparison with FLUGG and GCALOR simulations it was found convenient to group the cluster categories into the following four particle categories:

- **Particles with low energy transfer (LETP)**: dots + small blobs + curly tracks on the whole sensor;

2022 JINST 17 P01027

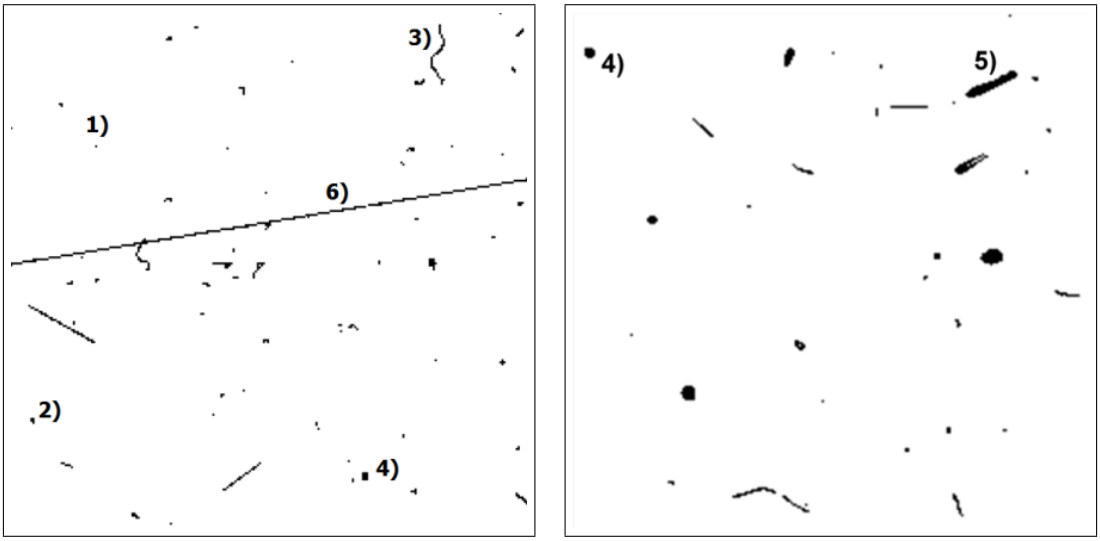

(a) (b)

Figure 3. a) Background measurement in the ATLAS cavern in 2008 before any collision period with MPX11 (low threshold of 10 keV, acquisition time of 100 min, for detector location see figure 2). b) Response under fast neutron irradiation in a cyclotron beam (wide energy spectrum from 2 to 30 MeV) at low threshold with acquisition time of 100 µs. The inserted labels 1 to 6 describe the assignment of clusters to individual interacting quanta of radiation by means of the pattern recognition algorithm as explained in the text.

- **Particles with high energy transfer (HETP)**: heavy blobs + heavy tracks on the whole sensor except below the ^{6}LiF region;
- **Minimum ionizing particles (MIPs)**: straight tracks on the whole sensor;
- **Thermal neutrons**: heavy blobs below the ^{6}LiF region.

2.3 Simulation of the cavern radiation field by FLUGG

An extended simulation geometry, which contains details of the ATLAS detector subsystems and parts of the LHC beam tunnels including two access shafts, is defined in section 2.3.1. Then scoring volumes are defined there. The generation of a simulation sample containing approximately 10^6 minimum-bias events is described in section 2.3.2. Primary particles from proton-proton (pp) interactions as well as secondary particles (including neutrons, electrons and photons from decay of activated nuclei) are scored until their energies are below user defined cuts. A summary of the number of particles recorded in each scoring volume sorted by particle type and particle categories is given in section 2.3.3. Section 2.3.4 is dedicated to the description of spectral distribution of neutrons in different regions of ATLAS.

2.3.1 The model

The first simulation used here is an application [13] based on FLUGG [14] developed for the study of radiation background in the ATLAS detector cavern. This application was initially validated against a similar program based on GCALOR (see section 2.4) by using the same geometry and same event

2022 JINST 17 P01027

generator as those in the Radiation Background Task Force Report [4]. The geometry description was then updated. It extends beyond the ATLAS cavern, and includes parts of the LHC beam tunnels and the two access shafts PX14 and PX16 as shown in figure 4. Information on vacuum chambers and beam line shielding is taken from the ATLAS Shielding Project web page [15]. As we are not concerned with the ATLAS detector response, much of the internal geometry detail of the detector subsystems has been simplified to increase simulation speed. Simulation results obtained with the updated geometry have been validated against hit rates in the Muon Spectrometer [16], RADMON measurements in the Inner Detector [17], and dosimeter measurements throughout the ATLAS detector [18].

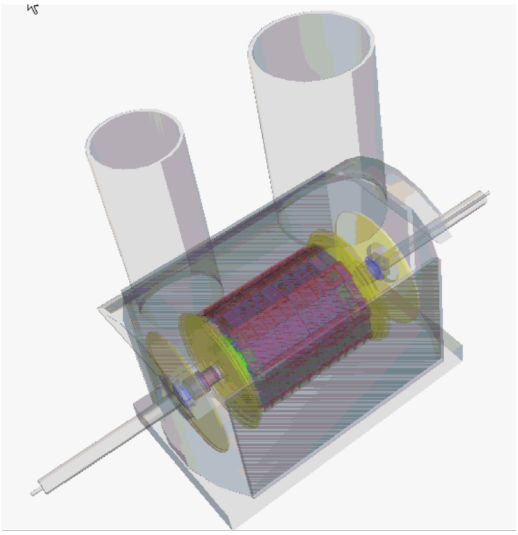

Figure 4. Geometry of the ATLAS cavern used in FLUGG application with visible access shafts PX14 and PX16.

The simulation program followed particles until their energies were below user defined cuts. The default energy cut values were 100 keV and 10 keV for electron and photons, respectively. The change of photon cuts to 10 keV and 1 MeV led to no significant changes to particle energy distributions. In addition to the prompt particles from the initial proton-proton (pp) interactions, their decays and products of their secondary interactions in the ATLAS environment, the simulation also included the effects of material activation and radioactive decays. The magnetic field was included in the simulation since it has substantial influence on the particle flux in some of the locations in the ATLAS cavern. Scoring volumes were imaginary cylindrical shells in the simulation geometry, and information was recorded when a particle entered them. This output is referred to as a 4-vector file. The information in the 4-vector file contained:

- Event number;
- Particle ID in FLUKA convention;
- Generation number assigned by simulation;
- Kinetic energy in GeV;
- Particle position (X, Y, Z) in cm;

2022 JINST 17 P01027

- Particle direction cosines;
- Time in seconds after pp interaction;
- Scoring volume ID;
- Position where particle was "born". This is the position where the simulation program begins tracking that particular particle;
- Flag indicating if this particle is the product of a neutron capture reaction.

2.3.2 Simulation sample

The input to the simulation was approximately 10^6 minimum-bias events generated by PHOJET [19] at a centre-of-mass energy $\sqrt{s} = 7$ TeV, corresponding to the beam conditions in 2010 and 2011. In this time period, the ATLAS LHC runs were performed in standard beam conditions, i.e. after the LHC was adjusted to provide stable beams, ATLAS "opened the gate" and started to take the data. The beams were tuned so, that the luminosity was as high as possible. A scoring volume was defined for each MPX detector. Using a volume of the same sizes as the physical dimensions of an MPX detector would yield few counts for each simulated pp interaction because of the small size of the detector. Instead, we took advantage of the approximate cylindrical symmetry of the simulation geometry, and defined cylindrical scoring volumes with a Z extent of 1 cm and a radial extent of 1 cm resulting in the total effective area of the scoring volumes higher by the factor of about 175 to 2000 than the MPX sensor with the area of 2 cm^2.

The final simulation sample available for use corresponded to 982 620 pp interactions. The 4-vector file for the 15 MPX scoring volumes contained roughly 1.3×10^8 entries from which 90% were scored for MPX15, 8.3% for MPX01 and MPX14, 1.65% for MPX02 and MPX13, and the remaining 0.5% for all other MPX detectors.

2.3.3 Particle types

Photons and neutrons were the most populous particle types among the 4-vectors. Their relative fractions depended on the MPX location. Table 2 summarizes the number of particles recorded in each scoring volume sorted by particle type and particle categories defined in section 2.2.4 which were used for the comparison with MPX measurements. Energy and angle limits for each particle group are stated later in section 3.

2.3.4 Neutron spectral fluence distributions

Figure 5 shows the spectral fluence distribution of neutrons for MPX01 and MPX14 (figure 5 left, black line), MPX02 and MPX13 (figure 5 left, red line) and MPX15 (figure 5 right). MPX01 and MPX14 have more high-energy neutrons but are similar to MPX02 and MPX13 for energies below 1 MeV. The distribution for MPX15 is significantly different from the other MPX detectors suggesting that the response of MPX15 below ^{6}LiF converter may be primarily caused by the ^{6}Li disintegrations initiated by fast neutrons (see section 3.3.2 for resonance integral correction of thermal neutron fluence for this effect).

2022 JINST 17 P01027

Table 2. Summary of particle numbers recorded in each FLUGG scoring volume sorted by particle type (including anti-particles) and particle categories, for 982 620 pp interactions.

MPX	Total number of recorded particles in scoring volume	Total number of neutrons	Total number of thermal neutrons with $E < 0.5$ eV	Total number of fast neutrons with $E > 0.5$ MeV	Total number of photons	Total number of electrons	Total number of protons	Total number of muons	Total number of charged pions	Total number of charged kaons	Total number of other particles	Number of LETP electrons	Number of LETP protons	Number of LETP muons	Number of LETP pions	Number of LETP kaons	Number of HETP protons + alphas + tritons + deuterons	Number of HETP muons	Number of HETP pions	Number of HETP kaons
01	5367480	1271459	207499	415912	3762737	156294	27724	18413	119570	7228	4055	153162	13646	16811	113955	7126	13866	1286	2151	89
02	1101439	603754	121169	94899	486395	8276	935	397	1510	80	92	7432	161	274	778	68	717	17	60	3
03	213166	124583	26949	17848	86695	1698	102	24	58	1	5	1645	5	8	31	0	87	1	5	0
04	167700	139142	21697	24091	27725	630	69	120	10	1	3	630	5	113	7	1	63	3	0	0
05	142445	108116	15351	11606	33638	603	42	40	2	1	3	602	1	39	0	1	40	0	0	0
06	101996	74316	10861	8211	27171	448	29	31	0	1	0	445	1	29	0	1	27	2	0	0
07	10131	7063	1359	397	3015	46	1	6	0	0	0	45	0	2	0	0	1	0	0	0
08	13507	9447	1628	681	3979	69	3	6	1	1	1	69	0	1	1	0	2	0	0	0
09	10855	6945	2477	624	3792	89	5	24	0	0	0	89	1	1	0	0	4	0	0	0
10	11409	6814	3872	538	4540	48	2	5	0	0	0	48	0	0	0	0	2	0	0	0
11	22370	14911	5970	877	7382	71	3	3	0	0	0	71	0	0	0	0	3	0	0	0
12	42410	27643	4562	3117	14306	346	80	17	18	0	0	338	1	4	2	0	77	3	1	0
13	1101712	602442	122270	94735	487821	8425	923	428	1501	86	86	7398	168	277	744	75	687	15	61	8
14	5360810	1270429	207724	414964	3758791	155454	27192	18498	119184	7146	4116	152272	13444	16837	113423	7064	13534	1335	2163	73
15	117727461	37290798	42663	7207753	74080198	6066444	68528	8781	189347	15157	8208	6055917	26376	8031	176385	14853	40706	421	3770	220

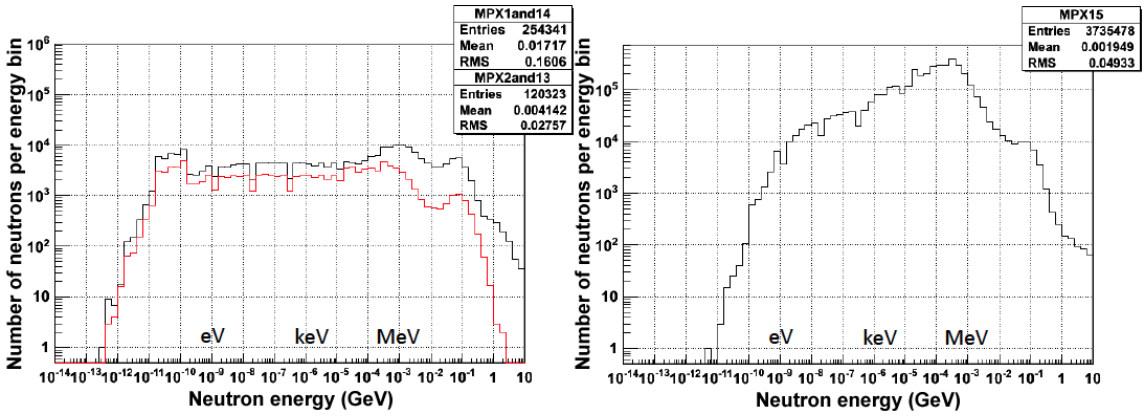

Figure 5. Spectral fluence distribution of neutrons entering MPX01 and 14 (left; black line), MPX02 and MPX13 (left; red line) and MPX15 (right) scoring volumes. X-axis represents energy in GeV and Y-axis is the number of neutrons per energy interval.

2.4 Simulation of the cavern radiation field by GCALOR

The second simulation utilized here is an application based on the PHOJET event generator and the Geant3/GCALOR [20] simulation originally used in 2003 for the study of background in the ATLAS detector cavern. The 2010 update of the simulation code contains improved detector description and a 16 m radius ATLAS cavern model. It was used to generate 4-vector files at the positions of MPX01-MPX12 and MPX15 [21]. MPX14 and MPX13 were assumed to be symmetrical to MPX01 and MPX02, respectively, therefore the values in tables 7, 9, and 13 are the same for these symmetrical detectors. The simulations followed all particles created in pp interactions at $\sqrt{s} = 7$ TeV and any subsequent interactions along their path through the ATLAS cavern up to their absorption as summarized in section 3.2.1. Magnetic field was included in the simulations. Every

2022 JINST 17 P01027

particle crossing a scoring volume was recorded and its type, energy, position and direction vector were stored in a 4-vector file. Scoring volumes were cylindrical shells around the beam axis either with several cm length and 1 mm thickness or with 1 mm length and several cm thickness, depending on the sensor chip orientation (figure 2 and table 1). The longer dimension of the shell was 1.4 cm (MPX15), 6.0 cm (MPX01-06), or 30 cm (MPX07-12) resulting in the total effective area of the scoring volumes higher by the factor of about 10^3 to 3.5×10^4 than the MPX sensor with the area of 2 cm^2. The GCALOR default energy cut values were 1 MeV and 10 keV for electrons and photons, respectively.

The scoring volumes were duplicated symmetrically to the interaction point to double the particle statistics. More detailed description of the simulations, including examples of neutron spectral fluence distributions, can be found in [5].

2.4.1 Particle types

Table 3 summarizes the number of particles recorded in each scoring volume sorted by particle type and particle categories defined in section 2.2.4. Energy and angle limits for each particle group are stated later in section 3.

Table 3. Summary of particle numbers recorded in each GCALOR scoring volume sorted by particle type (including anti-particles) and particle categories.

MPX	Number of pp collisions	Total number of recorded particles in scoring volume	Total number of neutrons	Total number of thermal neutrons with $E < 0.5$ eV	Total number of fast neutrons with $E > 0.5$ MeV	Total number of photons	Total number of electrons	Total number of protons	Total number of muons	Total number of charged pions	Total number of charged kaons	Total number of other particles	Number of LETP electrons	Number of LETP protons	Number of LETP muons	Number of LETP pions	Number of LETP kaons	Number of HETP protons + alphas + tritons + deuterons	Number of HETP muons	Number of HETP pions	Number of HETP kaons
01	131401	1131897	158644	437543	3403715	146144	33638	18828	131183	8994	4826	1131897	143795	18320	17373	127673	8909	15282	1100	1950	81
02	131261	219205	49182	39055	149228	1799	306	117	377	36	28	219205	1674	82	99	270	33	214	3	15	2
03	130519	27209	8003	7182	32559	572	43	8	22	0	0	27209	563	2	6	13	0	40	1	2	0
04	131166	138778	49465	13441	84627	828	75	144	5	0	0	138778	828	8	144	3	0	66	0	1	0
05	130897	68485	14094	5118	36486	369	23	45	2	1	0	68485	369	2	43	2	1	21	2	0	0
06	130889	47180	9227	4078	24550	271	28	37	4	0	0	47180	271	0	35	2	0	28	2	0	0
07	50403	13346	2928	2075	5172	73	8	21	0	0	0	13346	72	0	7	0	0	8	0	0	0
08	49887	11978	2505	1151	3611	47	1	28	1	0	0	11978	46	0	7	1	0	1	0	0	0
09	48975	4860	1499	1253	4498	41	12	5	0	0	0	4860	41	0	1	0	0	11	1	0	0
10	49836	8664	3335	922	4179	33	5	8	0	0	0	8664	33	2	2	0	0	2	0	0	0
11	50524	35961	15779	3681	16012	106	4	3	0	0	0	35961	106	2	3	0	0	2	0	0	0
12	50887	42345	9001	6350	24291	56	54	14	2	0	0	42345	56	0	3	0	0	49	0	0	0
15	5994	594878	829	102147	975447	54359	1140	135	3231	216	114	594878	54315	575	129	3114	214	562	4	65	2

2.5 Simulation of the MPX device response by MCNPX

Supplemental Monte Carlo simulations were performed in order to obtain MPX detector energy and angular detection efficiencies to photons, thermal and fast neutrons, electrons, protons, muons, and charged pions. All details of the MPX detector are described in section 3.3.1. Such data were used to convert the simulated particle numbers from FLUGG and GCALOR 4-vector files into MPX cluster counts. In the case of thermal neutrons, the simulated detection efficiencies were also used to estimate the anisotropy correction for the thermal neutron fluence. The simulations were done

2022 JINST 17 P01027

utilizing the general-purpose Monte Carlo code MCNPX in version 2.7.E [12]. Section 3.3.2 is dedicated to validation of the MPX detector model.

2.5.1 The MPX device model

The model reproduced details of the MPX detector (figure 6). It included a duralumin box with the entrance window, all converter layers (polyethylene, aluminium, ^{6}LiF, and their combinations), sensor chip, bonding, readout chip, printed circuit board, etc. For calculation of the energy and angular detection efficiencies, a mono-directional and mono-energetic source was rotated around the detector longitudinal axis, in 15° steps. The area of the source was 15 cm × 6 cm corresponding to the dimensions of the MPX duralumin box in order to account for scatter in the MPX detector material. Particle energies were selected in such a way that the resulting detection efficiencies allowed accurate linear interpolation between energies and angles.

The detection efficiency $\varepsilon(P, E, \Theta)$ for particle P with energy E and incidence angle Θ was calculated according to eq. (2.1):

$$\frac{N_{\mathrm{src}}(P, E, \Theta)}{S_{\mathrm{src}}} = \frac{N_{\mathrm{det}}(P, E, \Theta)}{S_{\mathrm{det}} \times \varepsilon(P, E, \Theta)} \tag{2.1}$$

where $N_{\mathrm{src}}(P, E, \Theta)$ is number of simulated source particles, S_{src} is the area of the source, $N_{\mathrm{det}}(P, E, \Theta)$ is the number of simulated counts in the detector pulse-height spectrum above a deposited energy threshold, and S_{det} is the area of the sensitive part of the sensor (e.g., area below ^{6}LiF in thermal neutron simulations). Plots of the energy-angular detection efficiencies for all particles of interest can be found in [5].

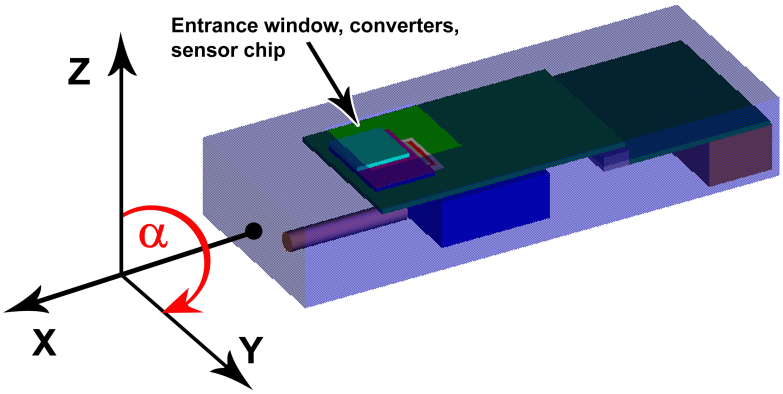

Figure 6. Visualization of the detailed model of the MPX device. The duralumin box ($14.5 \times 6.0 \times 2.5\,\mathrm{cm}^3$) is set to be semi-transparent to view the inner structure. Position of the sensor chip, partly covered by converter layers, is marked by the arrow.

2.5.2 Validation

Validation of the MPX model was performed in order to ensure that the Monte Carlo method used for determination of the simulated MPX detection efficiencies provided reliable results. It was done for the following particles and measurement geometries for which the geometry can be easily modelled and both measurement and simulation results can be clearly interpreted:

- isotropic field of thermalized neutrons;
- fast neutron beam from an ^{241}AmBe neutron source (mean energy 4.16 MeV);
- photon beam from ^{60}Co (mean energy 1.25 MeV) and ^{137}Cs (mean energy 662 keV) radionuclide sources.

Because all the MPX detectors were already installed in the ATLAS cavern at the time of Monte Carlo model validation, the measurements were performed using two back-up detectors with identification numbers K06-W0048 and G05-W0045. These detectors were of the same type and included the same converter layout as the MPX detectors. The measurements were performed at the Czech Metrology Institute, Prague, in the reference radiation fields with the lowest uncertainty on dosimetric quantities available in the Czech Republic. All measurements were done in low threshold mode of detector operation (see section 2.1.3).

The measurement of thermal neutron detection efficiency was performed inside a graphite prism where an isotropic field of thermalized neutrons is achieved. The thermal neutron flux was $(32.0 \pm 1.6) \times 10^3$ neutrons/cm^2/s and the cadmium ratio of the thermalized neutron field was 21.5. The measured quantity was the number of heavy blobs below the ^{6}LiF converter, which was recalculated into the detection efficiency using a formula similar to eq. (2.1). Table 4 presents the comparison of measured and simulated thermal neutron detection efficiency.

Table 4. Results of the MPX model validation for an isotropic thermal neutron source. Uncertainty is only statistical.

Sensor ID	Detection efficiency
Measurement, K06-W0048	$(0.94 \pm 0.05)\%$
Measurement, G05-W0045	$(1.25 \pm 0.06)\%$
Simulation, $E_{\mathrm{cut}} = 230$ keV	$(1.11 \pm 0.01)\%$

The measurement of the fast neutron detection efficiency was performed with a ^{241}AmBe source with a neutron emission of $(21.6 \pm 0.2) \times 10^6$ neutrons/s. The measured quantity was the number of heavy blobs and heavy tracks below the polyethylene convertor and in the uncovered region, which was recalculated into the detection efficiency. Table 5 presents the comparison of the measured and simulated detection efficiency. The simulation gives approximately 10% higher efficiencies, than the measurement.

Table 5. Results of MPX model validation for ^{241}AmBe fast neutron source. Uncertainty is only statistical.

	Detection efficiency	
Sensor ID	polyethylene minus uncovered	polyethylene
Measurement, K06-W0048	$(0.086 \pm 0.005)\%$	$(0.121 \pm 0.004)\%$
Measurement, G05-W0045	$(0.075 \pm 0.004)\%$	$(0.117 \pm 0.004)\%$
Simulation, $E_{\mathrm{cut}} = 230$ keV	$(0.090 \pm 0.002)\%$	$(0.133 \pm 0.001)\%$

For photons, the comparison between simulation and measurement was performed for a value of a conversion coefficient from the LETP cluster count into the radiation protection quantity ambient

2022 JINST 17 P01027

dose equivalent rate, $H^*(10)$ [5]. The detector was positioned perpendicularly to the ^{60}Co and ^{137}Cs photon beam axis, and irradiated from the front side or from the back side. The detector was uncovered so the electrons created by photons in the air and surroundings could contribute to the measured signal as well, in addition to electrons created directly in the sensor chip. The reference air-kerma rate of the photon beams at the MPX detector position was converted into $H^*(10)$ using tabulated conversion coefficients [22] and divided by the corresponding LETP cluster count. Table 6 presents the comparison of measured and simulated values of the conversion coefficient.

Table 6. Results of MPX model validation for photons from ^{60}Co and ^{137}Cs sources. Uncertainty is only statistical.

	Conversion coefficient (Sv/cluster)	
Sensor ID, photon source	**Irradiation from the front**	**Irradiation from the back**
Measurement, G05-W0045, ^{137}Cs	(1.72 ± 0.06)E−10	(1.79 ± 0.06)E−10
Simulation (E_{cut} = 8 keV), ^{137}Cs	(1.88 ± 0.03)E−10	(1.94 ± 0.04)E−10
Ratio simulation/measurement, ^{137}Cs	1.09 ± 0.04	1.08 ± 0.04
Measurement, G05-W0045, ^{60}Co	(2.29 ± 0.15)E−10	(2.39 ± 0.15)E−10
Simulation (E_{cut} = 8 keV), ^{60}Co	(2.49 ± 0.04)E−10	(2.65 ± 0.05)E−10
Ratio simulation/measurement, ^{60}Co	1.09 ± 0.07	1.11 ± 0.07

In all cases the simulation gives approximately 9% higher values of the conversion coefficient. This means that the simulated detection efficiency (simulated cluster count) is lower. It could be caused by too high energy cut value or by a simplification of the model, which neglected scattering objects, like irradiation hall walls and floor or a detector holder. Also, the discrepancy could be caused by the difference between the used and real photon fluence spectra. Taking into account all unknown parameters of the measurement conditions and the simulation simplifications, the agreement between the simulation and measurement is satisfactory and sufficient for the purpose of comparison of the ATLAS cavern radiation background.

3 Results

In this section the results of the comparison are given together with a detailed description of procedures used. Attention is devoted to the analysis of statistical uncertainties as well as to corrections of systematic errors resulting from the random overlapping of particle tracks. The simulation and measurement data used for the comparison are described in sections 3.1 and 3.2, respectively. Sections 3.3–3.5 deal with the comparison of different categories of particles — thermal neutrons, LETP and HETP, respectively.

3.1 Simulation data used for the comparison

The FLUGG and GCALOR simulation data consist of 4-vectors for all particles entering the scoring volumes. The structure of a FLUGG 4-vector file is described in section 2.3.1. The structure of a GCALOR 4-vector file was similar.

By analysing this 4-vector file and filtering particles with proper characteristics, it was possible to estimate values of simulated LETP and HETP cluster counts and thermal neutron fluences which

2022 JINST 17 P01027

could be compared to MPX measurements, with one exception: the thermal neutron fluence from FLUGG simulation was calculated directly by the FLUGG code. A procedure for the estimate of the simulated quantities mentioned above consisted of the following four main steps:

- At first, the 4-vector files were filtered and only the particles with the energy and incidence angle matching the criteria for the given fluence/cluster count were selected. The criteria are listed in sections 3.3.1, 3.4.1 and 3.5.1 for the thermal neutron fluence, LETP cluster count and HETP cluster count, respectively. Incidence angle is an angle between the particle direction vector and positive normal of the sensor chip surface. The criterion value for angle cut-off is based on the requirement of the pattern recognition algorithm that, not to be considered as a MIP, a particle must leave a straight path less than 20 pixels long. The criterion value for the energy cut-off is derived from the collision stopping power, $\mathrm{d}E/\mathrm{d}x$, of charged particles in silicon. Based on current experience with MPX detectors and on complementary measurements performed in proton beams in the Heidelberg Ion-Beam Therapy Center (HIT) of the German Cancer Research Center (DKFZ) in 2013, it is assumed that charged particles with collision stopping power lower than approximately 87 keV per 55 µm (the pixel width of the MPX sensor) do not create tracks which are recognized by the pattern recognition algorithm as a heavy blob or as a heavy track assigned to the HETP group (see section 3.4.4 for more details). The influence of this $\mathrm{d}E/\mathrm{d}x$ cut on the results of the comparison is discussed in sections 3.4.4 and 3.5.4;

- Subsequently, detection efficiency was assigned to every filtered particle. The detection efficiency was taken from a pre-computed database of the energy-angular detection efficiencies of MPX device according to the particle type and its energy and incidence angle. Such energy-angular detection efficiencies are known from MCNPX Monte Carlo simulations for each particle type considered in the comparison (section 2.5). The procedure took into account the real detection probability of the MPX device allowing one to obtain the most precise recalculation from simulated particle energy-angular flux distribution into the detector signal. Due to the rectangular section of scoring volumes in GCALOR simulations, a weighting factor for particles entering the volume from a thinner side was applied as a ratio of rectangle side lengths [5];

- Next, the detection efficiencies of all filtered particles were summed to obtain the total simulated LETP or HETP cluster count or thermal neutron fluence;

- Finally, the total simulated LETP or HETP cluster count or thermal neutron fluence is normalized to unit area of the scoring volume and to unit luminosity by multiplying the value by a constant c given in eq. (3.1):

$$c = \frac{\sigma \times 10^9}{N \times S} \tag{3.1}$$

where σ is the inelastic pp interaction cross section at $\sqrt{s} = 7$ TeV, $\sigma = 71$ mb [23], N is the number of pp collisions in FLUGG ($N = 982620$) or GCALOR (N depends on MPX detector, see table 3) simulation, 10^9 is the recalculation of the number of pp collisions for an integrated luminosity of 1 nb^{-1}, and S is the area of the scoring volume annulus in FLUGG or GCALOR simulations calculated as $\pi(R^2_{\mathrm{max}} - R^2_{\mathrm{min}})$ for MPX detectors oriented perpendicularly to the

2022 JINST 17 P01027

Z-axis (MPX01-06 and MPX13-15) and as $2\pi R(Z_{\max} - Z_{\min})$ for detectors oriented parallel to the Z-axis (MPX07-12). $R_{\min}$, $R_{\max}$ and R are the inner, outer and mean radius of the scoring volume annulus, respectively, and $(Z_{\max} - Z_{\min})$ is the scoring volume thickness in the Z-direction.

The relative uncertainty on the simulation fluence/cluster count Y was calculated by eq. (3.2) assuming the Poissonian, $\sigma = \sqrt{(N_{\mathrm{i}})}$, $\sigma_{\mathrm{rel}} = 1/\sqrt{(N_{\mathrm{i}})}$, distribution of statistical uncertainties:

$$\sigma_{\mathrm{rel}}(Y) = \frac{1}{\sqrt{\sum_i (\sqrt{N_i})^2}} \tag{3.2}$$

where N_i is the number of filtered particles of type i counted into the quantity Y.

3.2 Measurement data used for the comparison

The luminosity measured with the ATLAS luminosity detector [24] was utilized. Integrated luminosity used for data normalization is the sum of luminosity in each luminosity block in the collision period. The collision period refers to the time interval between the beginning and end of continuous beam (proton-proton) collisions when MPX detectors observe significantly higher cluster rate than the background cluster rate. It corresponds to a "fill" rather than to a "run". The start and end time of each collision period was determined from the response of MPX detectors, i.e., independently of any other ATLAS measurements.

Cluster counts and fluences were calculated independently for each collision period and then the average value over all collision periods was determined. The statistical uncertainty on the number of detected clusters in each collision period was typically between 0.01% and 0.5%, depending on the MPX detector position and cluster type. More details can be found in [5].

3.2.1 Correction for overlapping tracks

In the tracking mode of MPX detector operation, when many clusters were recorded in a single frame, particle tracks occasionally and randomly overlapped resulting in the underestimation of the number of clusters by the pattern recognition algorithm. For each MPX detector, for each type of clusters, and independently for the ^{6}LiF region of the sensor and the rest of the sensor, a separate empirically found correction to account for overlapping tracks was obtained and utilized to compensate for this effect.

Every correction function was determined from suitable data measured by the given MPX detector during a collision period. Usually, several thousands of frames with mean total cluster count per frame of 60 clusters were used and summed together step by step to achieve up to roughly 1000 original clusters per one summed frame. In each step the cluster count recognized by a pattern recognition algorithm in all summed frames was recorded to obtain a relation between the recognized and the correct mean cluster count per frame. The ratio of the correct and the recognized mean cluster count per frame per unit area, in dependence on the recognized mean cluster count per frame per unit area, is the desired correction. As an example, for selected MPX detectors the figure 7 presents this correction for heavy blobs used for calculation of thermal neutron fluence per unit luminosity.

Depending on the MPX detector and on the radiation field at its location the corrections are reliable up to the total of roughly 300 to 400 clusters/frame/cm^2. Measurement data used for the comparison were obtained in much lower total cluster counts/frame/cm^2, usually below

2022 JINST 17 P01027

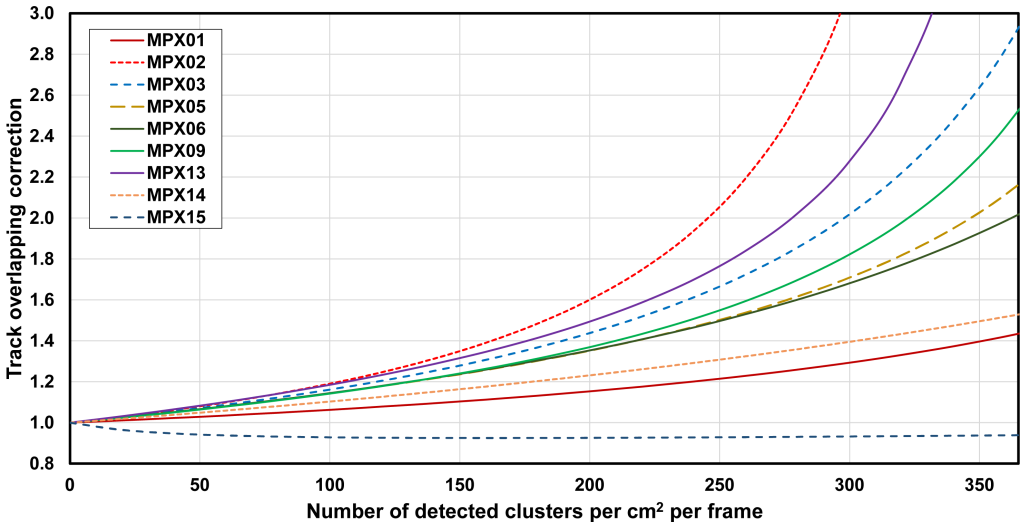

Figure 7. The correction for overlapping tracks for heavy blobs used for calculation of thermal neutron fluence per unit luminosity. The correction for MPX detectors not presented here lies between MPX03 and MPX06.

150 clusters/frame/cm^2. Figure 8 shows an example of the overlapping tracks correction applied to MPX05 heavy blobs used for calculation of thermal neutron fluence per unit luminosity. The correction value depends on the LHC instantaneous luminosity. As the luminosity was increasing in time in the presented figure 8, the correction was increasing as well.

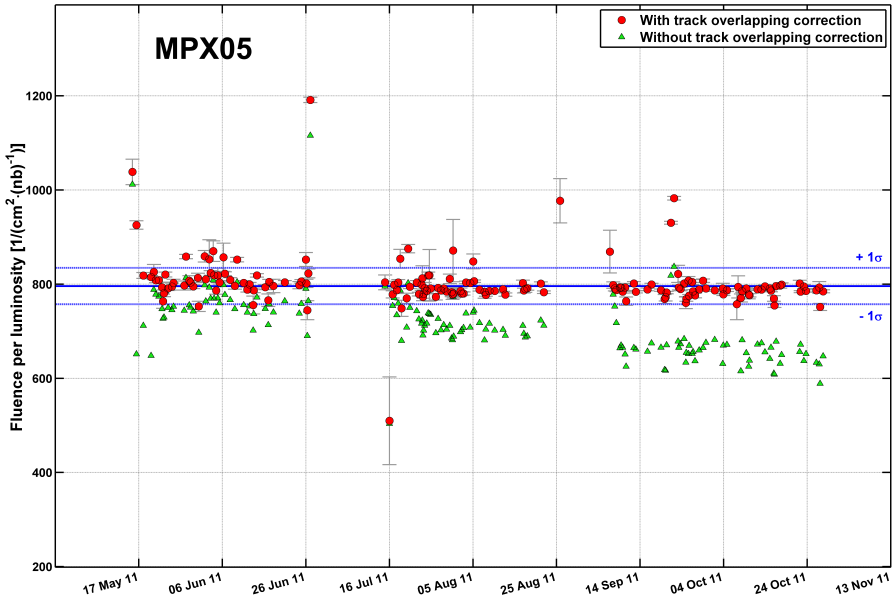

Figure 8. Example of thermal neutron fluence per unit integrated luminosity between 15 May 2011 and 28 October 2011 for each collision period for MPX05. Values corrected (red circles) and uncorrected (green triangles) for overlapping tracks are shown. The correction depends on the number of overlapping tracks on each frame, i.e. on the instantaneous luminosity. Scattered (really off) points are caused by short collision periods or by unavailable luminosity data.

2022 JINST 17 P01027

3.3 Thermal neutrons

In this section the simulation and measurement input data used for the comparison of thermal neutrons are defined.

3.3.1 Simulation data

All neutrons with energy below 0.5 eV were considered to be thermal. FLUGG thermal neutron fluence was calculated directly by the software, GCALOR thermal neutron fluence was obtained by a procedure described in section 3.1.

3.3.2 Measurement data

Thermal neutrons were defined as all neutrons with energy below 0.5 eV which is approximately the energy of the so-called "cadmium edge", i.e., edge energy for high cross section for neutron capture on ^{113}Cd. MPX devices detect thermal neutrons effectively via charged ions from the nuclear reaction (eq. (3.3) [25]):

$$\mathrm{n} + {}^{6}\mathrm{Li} \rightarrow \alpha(2.05\,\mathrm{MeV}) + {}^{3}\mathrm{H}(2.73\,\mathrm{MeV}); \quad \sigma(25\,\mathrm{MeV}) = 940\,b \tag{3.3}$$

in a thin ^{6}LiF conversion layer deposited under an Al foil (see figure 1) placed above the sensor chip. After the absorption of a neutron, the ^{6}Li nucleus disintegrates into two heavy charged particles, a triton and an alpha particle, which may subsequently enter the sensor chip and cause signal recognized as a heavy blob. The thermal neutron fluence per unit luminosity is then calculated from the difference between the number of heavy blobs below the ^{6}LiF and Al converters according to eq. (3.4):

$$\Phi_j = K_{ri} \times K_a \times \frac{1}{L_j} \times \frac{(t_2)_j - (t_1)_j}{\sum_{k=(t_1)_j}^{(t_2)_j} T_k} \times \frac{\sum_k (N_{\mathrm{HB}}^{LiF})_k}{\varepsilon \times S_{\mathrm{LiF}}} \times \left(1 - \frac{S_{\mathrm{LiF}}}{S_{\mathrm{Al}}} \times \frac{\sum_k (N_{\mathrm{HB}}^{Al})_k}{\sum_k (N_{\mathrm{HB}}^{LiF})_k}\right) \tag{3.4}$$

where Φ_j is the thermal neutron fluence per unit integrated luminosity calculated from the frames recorded during the j-th collision period, $(N_{\mathrm{HB}})_k$ is the number of heavy blobs under Al or LiF convertor in the k-th frame during the j-th collision period. This number is already corrected for the overlapping tracks (see section 3.2.1). K_{ri} is the correction to the resonance integral, K_a is the correction to the thermal neutron field anisotropy, L_j is the integrated luminosity during the j-th collision period, $S_{\mathrm{LiF/Al}}$ is the area of the Al or LiF convertor, ε is the thermal neutron detection efficiency as obtained from the measurements in isotropic thermal neutron calibration field, T_k is the acquisition time of the k-th frame during the j-th collision period, and t_{1j}, t_{2j} is the start and end time of the j-th collision period, respectively [5].

Eq. (3.4) includes the normalization to the unit integrated luminosity, correction to the detector real measurement time, the conversion from cluster count to fluence, and the subtraction of the background, i.e., heavy blobs below ^{6}LiF layer not caused by ^{6}Li disintegrations during the collisions. The heavy blobs caused by thermal neutrons should occur during collision periods and a few seconds after the collision periods end until the thermalized neutrons are absorbed. However, the background counts for other particle types (section 3.4.2) were calculated in time intervals starting 30 min after the end of collision periods, therefore no thermal neutron background from the non-collision period measurement was subtracted here. The measured thermal neutron background flux is presented in [5]. Within the measured uncertainties, the background flux is zero in most MPX detectors.

2022 JINST 17 P01027

Eq. (3.4) also includes two additional corrections: the resonance integral correction, K_{ri}, and thermal neutron field anisotropy correction, K_a. The resonance integral correction corrects for the signal from ^{6}Li(n,α) reaction caused by neutrons with energy higher than 0.5 eV. A resonance integral is an integral of the product of neutron spectral fluence and neutron cross section for the (n,α) interaction over a given neutron energy range. The ratio of two resonance integrals, the first calculated from 0 to 0.5 eV and the second calculated over all neutron energies, gives the value of the correction K_{ri} [5]. Measured thermal neutron fluences presented in table 7 were corrected to the resonance integral using spectral fluence distributions from the FLUGG simulations (see figure 5 presenting the spectral fluence distributions for MPX01, 02, and 15). The resonance integral corrections varied from −2% to −15% (i.e., the final value of thermal neutron fluence was lower) except for MPX15 where the correction reached −91% due to the lack of thermal neutrons in the neutron spectrum (figure 5). This was caused by the presence of a huge amount of iron that has high absorption cross section for neutrons. Corrections calculated from GCALOR neutron spectra would be similar, including the −91% correction for MPX15.

The anisotropy correction accounts for the thermal neutron field anisotropy, or, more precisely, for the difference between the MPX detector response in the isotropic thermal neutron calibration field and a real thermal neutron field in the ATLAS cavern at a position of the given MPX detector. In ATLAS, the anisotropy is caused by huge amount of materials and a position of most MPX detectors which are very close to concrete walls, cable trays, or other massive objects. The correction procedure utilizes the FLUGG simulated distribution of thermal neutron direction vectors available in 4-vector files and MCNPX calculated angular-dependent detection efficiencies for thermal neutrons. A full description of this correction can be found in [5]. The correction varies from +8% to -7% except for MPX01 and MPX14 where the correction reached −19% (i.e. the final value of the thermal neutron fluence was lower). Corrections calculated from GCALOR neutron spectra were practically the same, including the -19% correction for MPX01 and MPX14. Values of both corrections, calculated from FLUGG data, are presented in table 7.

The final value of measured thermal neutron fluence per unit integrated luminosity was calculated as a weighted mean of the fluences obtained for each collision period.

3.3.3 Comparison of measurement and simulation

Comparison for the thermal neutron fluence per unit integrated luminosity of all 15 MPX detectors is summarized in table 7 and figures 10–12. Measured and simulated fluences generally agree within a factor of two, with the exception of MPX07 and MPX09-11 where the simulated fluences are higher. The significant discrepancy for MPX11 is not so important for the overall result of the comparison because MPX11 is located on the cavern wall far from the beam line (see figure 2) where the models, especially GCALOR model, are not defined in detail. There is also a larger discrepancy in the FLUGG thermal neutron fluence in MPX03. However, it has to be stressed that the thermal neutron fluence is significantly influenced by the material surrounding the detector i.e. bunch of cables, concrete walls, steel frames, etc. (figure 9). There is also a discrepancy between the measurement in symmetrical detectors MPX02 and MPX13, reaching approximately 40%. However, MPX02 is positioned in a slightly different place than MPX13 and it is located beyond a steel plate. As it will be noticed in the following sections, the 40% difference in response of both detectors is observed

2022 JINST 17 P01027

in LETP and HETP cluster counts as well. That is why the discrepancy cannot be caused by the detectors themselves but rather by differences in the radiation fields at the positions of both detectors.

Figure 9. Example of the location of an MPX detector in ATLAS: MPX03 is fixed on a metal plate and surrounded by a batch of cables made of various materials which may have a significant influence on local radiation field at the position of the given MPX detector.

Table 7. Comparison of the average thermal neutron fluence per unit integrated luminosity measured by the MPX detectors and simulated by FLUGG and GCALOR Monte Carlo codes.

Detector	MPX measurement, Φ/L [cm^{-2}/nb^{-1}] (1)	FLUGG simulation, Φ/L [cm^{-2}/nb^{-1}] (2)	Ratio FLUGG / MPX	GCALOR simulation, Φ/L [cm^{-2}/nb^{-1}]	Ratio GCALOR / MPX (3)	Resonance integral correction (4)	Anisotropy correction (4)
MPX01	(3.45 ± 0.32)E+04	(3.13 ± 0.04)E+04	0.91 ± 0.09	(2.96 ± 0.01)E+04	0.86 ± 0.08	−10%	−19%
MPX02	(1.83 ± 0.09)E+03	(5.73 ± 0.06)E+03	3.13 ± 0.16	(2.90 ± 0.01)E+03	1.58 ± 0.08	−10%	8%
MPX03	(2.60 ± 0.15)E+02	(8.70 ± 0.21)E+02	3.35 ± 0.21	(3.23 ± 0.04)E+02	1.23 ± 0.07	−13%	4%
MPX04	(3.28 ± 0.11)E+03	(1.88 ± 0.04)E+03	0.57 ± 0.02	(5.48 ± 0.02)E+03	1.54 ± 0.05	−11%	4%
MPX05	(6.79 ± 0.27)E+02	(7.10 ± 0.25)E+02	1.05 ± 0.05	(7.71 ± 0.06)E+02	1.03 ± 0.04	−13%	−3%
MPX06	(1.82 ± 0.06)E+02	(3.62 ± 0.13)E+02	2.00 ± 0.10	(3.95 ± 0.04)E+02	1.99 ± 0.07	−15%	−7%
MPX07	(6.22 ± 0.36)E+00	(3.31 ± 0.13)E+01	5.33 ± 0.38	(4.76 ± 0.09)E+01	7.42 ± 0.45	−14%	0%
MPX08	(1.64 ± 0.06)E+01	(4.20 ± 0.28)E+01	2.56 ± 0.20	(4.31 ± 0.09)E+01	2.38 ± 0.10	−14%	2%
MPX09	(2.78 ± 0.13)E+01	(1.83 ± 0.17)E+02	6.58 ± 0.67	(7.39 ± 0.19)E+01	2.82 ± 0.15	−6%	0%
MPX10	(2.09 ± 0.08)E+01	(8.36 ± 0.46)E+01	3.99 ± 0.27	(4.85 ± 0.08)E+01	2.62 ± 0.11	−2%	3%
MPX11	(2.90 ± 0.28)E+00	(4.07 ± 0.27)E+01	14.02 ± 1.64	(7.05 ± 0.06)E+01	24.18 ± 2.37	−4%	1%
MPX12	(5.94 ± 0.21)E+01	(8.44 ± 0.33)E+01	1.42 ± 0.08	(1.07 ± 0.01)E+02	1.63 ± 0.06	−12%	1%
MPX13	(2.94 ± 0.12)E+03	(5.75 ± 0.03)E+03	1.96 ± 0.08	(2.90 ± 0.01)E+03	0.98 ± 0.04	−10%	7%
MPX14	(2.95 ± 0.16)E+04	(3.10 ± 0.03)E+04	1.05 ± 0.06	(2.96 ± 0.01)E+04	1.01 ± 0.05	−10%	−19%
MPX15	(1.80 ± 0.33)E+04	(2.47 ± 0.05)E+04	1.37 ± 0.25	(5.39 ± 0.19)E+04	2.93 ± 0.54	−91%	0%

(1) Including resonance integral, anisotropy and overlapping tracks corrections;
(2) Values directly from FLUGG calculations, the uncertainty calculated from eq. (3.2);
(3) Related to the MPX measurements corrected to the resonance integral and anisotropy obtained from GCALOR neutron spectral and angular fluence distributions;
(4) Calculated from FLUGG neutron spectral and angular fluence distributions.

2022 JINST 17 P01027

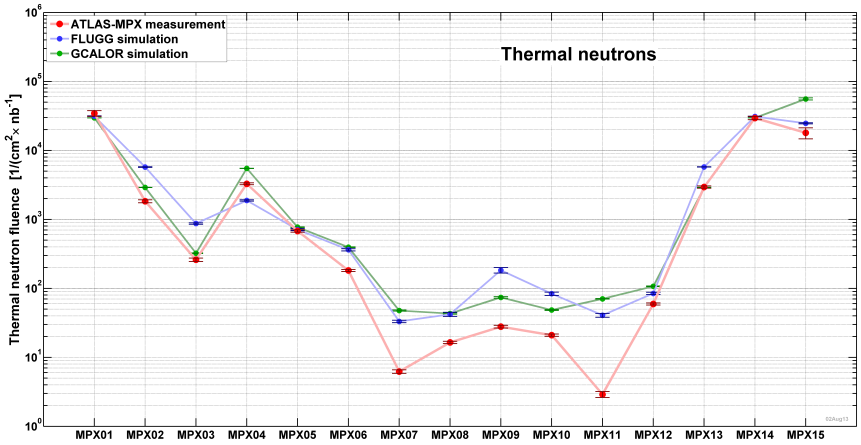

Figure 10. Comparison of thermal neutron fluence per unit integrated luminosity as measured by MPX detectors (red) and simulated by FLUGG (blue) and GCALOR (green). The lines are to guide the eye.

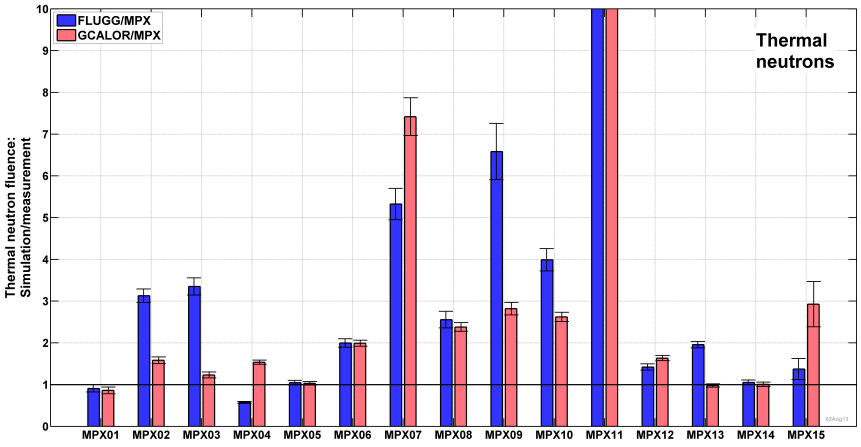

Figure 11. Ratio of simulated and measured thermal neutron fluence per unit integrated luminosity. FLUGG simulation is blue, GCALOR simulation is red.

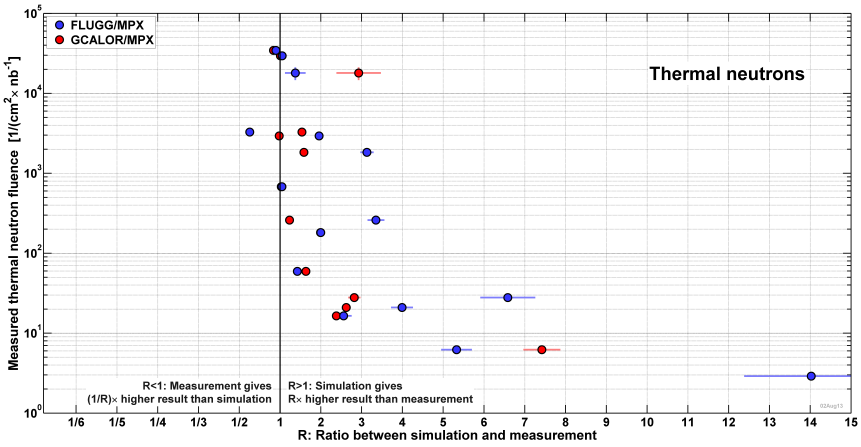

Figure 12. Ratio of simulated and measured thermal neutron fluence per unit integrated luminosity. FLUGG simulation is blue, GCALOR simulation is red.

3.4 Low energy transfer particles

In this section the input simulation and measured data used for the comparison of LETP are defined.

3.4.1 Simulation data

The following particles (and their anti-particles) stored in 4-vector files were selected and counted into the simulated Low Energy Transfer Particles (LETP) cluster count with the weight equal to their pre-calculated energy-angular detection efficiency (section 2.5):

- Electrons of all energies with incidence angle $< 75°$;
- Electrons with energy $E < 20\,\text{MeV}$ and incidence angle $> 75°$;
- Photons of all energies (photons can cause signal in the sensor through photo-atomic interactions in the sensor and in other materials if the recoiled electrons get into the sensor);
- Protons with energy $E > 80\,\text{MeV}$ and incidence angle $< 75°$;
- Muons with energy $E > 9\,\text{MeV}$ and incidence angle $< 75°$;
- Charged pions with energy $E > 12\,\text{MeV}$ and incidence angle $< 75°$;
- Charged kaons with energy $E > 42\,\text{MeV}$ and incidence angle $< 75°$;
- Fast neutrons (a fast neutron causes an LETP signal if the energy deposition in the sensor chip is higher than 8 keV but lower than roughly 230 keV, i.e., mostly through interactions with silicon nuclei in the sensor chip by elastic recoil, less through protons recoiled by fast neutrons in the polyethylene conversion layer. Such energy deposition has an importance for radiation damage comparable to that of HETP particles; however, it is counted into LETP cluster count because this energy deposition results in a cluster recognized as a dot or a small blob in MPX detectors).

The relative contribution of different particle types counted into the simulated LETP cluster count in every MPX detector is shown in table 8. The uncertainty is not presented. However, it can be roughly estimated from the number of particles counted into the LETP cluster count presented in tables 2 and 3. Both simulations are consistent, except for few differences, e.g. MPX04 and several MPX detectors with low statistics of simulated data.

3.4.2 Measurement data

Studies with FLUGG and GCALOR simulations showed that the main contribution to the LETP group comes from electrons and photons (table 8). These create a dot, a small blob, or a narrow curly track in the MPX detector. Highly energetic particles contribute to the measured LETP cluster counts if their incidence angle is $< 75°$ and if their collision stopping power in silicon is lower than approximately 87 keV per 55 µm.

2022 JINST 17 P01027

Table 8. Relative contribution of particles into the total simulated LETP cluster count.

	FLUGG simulation							GCALOR simulation						
	Photons	**Electrons**	**Muons**	**Pions**	**Protons**	**Kaons**	**Neutrons**	**Photons**	**Electrons**	**Muons**	**Pions**	**Protons**	**Kaons**	**Neutrons**
MPX01	11.5%	34.6%	5.8%	38.9%	6.3%	2.6%	0.4%	13.7%	34.4%	4.8%	36.7%	7.8%	2.7%	0.5%
MPX02	56.8%	24.7%	3.0%	7.6%	3.2%	0.8%	4.0%	65.0%	23.4%	2.2%	5.4%	2.2%	1.8%	5.9%
MPX03	67.2%	25.8%	0.4%	1.4%	0.8%	0.0%	4.4%	68.2%	30.1%	0.5%	0.8%	0.5%	0.0%	4.8%
MPX04	41.8%	21.8%	20.1%	0.7%	2.9%	0.2%	12.6%	75.3%	12.8%	10.9%	0.1%	0.9%	0.0%	4.6%
MPX05	56.2%	27.8%	7.5%	0.0%	1.1%	0.2%	7.2%	70.7%	23.6%	5.0%	0.2%	0.4%	0.1%	3.3%
MPX06	61.6%	22.8%	7.5%	0.0%	1.1%	0.3%	6.7%	58.4%	28.1%	13.0%	0.2%	0.4%	0.0%	4.0%
MPX07	71.9%	19.8%	4.1%	0.0%	0.0%	0.0%	4.3%	79.8%	15.0%	4.4%	0.0%	0.9%	0.0%	13.0%
MPX08	75.1%	17.1%	1.6%	0.7%	0.0%	0.0%	5.4%	80.3%	15.1%	4.0%	0.5%	0.0%	0.0%	8.1%
MPX09	71.9%	23.0%	0.8%	0.0%	0.7%	0.0%	3.6%	84.8%	12.0%	0.8%	0.0%	2.5%	0.0%	10.8%
MPX10	85.7%	11.1%	0.0%	0.0%	0.0%	0.0%	3.2%	77.1%	20.4%	1.1%	0.0%	1.5%	0.0%	3.3%
MPX11	85.2%	11.5%	0.0%	0.0%	0.0%	0.0%	3.2%	98.0%	0.7%	0.9%	0.0%	0.5%	0.0%	4.7%
MPX12	74.9%	17.5%	1.4%	1.0%	0.2%	0.0%	5.1%	96.7%	2.5%	0.5%	0.0%	0.3%	0.0%	7.0%
MPX13	57.3%	24.9%	2.9%	7.0%	3.0%	0.9%	4.0%	65.0%	23.4%	2.2%	5.4%	2.2%	1.8%	5.9%
MPX14	11.5%	34.5%	5.8%	38.9%	6.3%	2.6%	0.4%	13.7%	34.4%	4.8%	36.7%	7.8%	2.7%	0.5%
MPX15	13.8%	80.0%	0.2%	4.2%	0.9%	0.4%	0.7%	14.2%	78.6%	0.2%	5.1%	1.5%	0.4%	0.7%

The LETP cluster count was calculated independently for each collision period according to eq. (3.5):

$$(M_{\mathrm{A}})_j = \frac{1}{L_j} \times \frac{1}{S_{\mathrm{B}}} \times \left[\left(\sum_{i=(t_1)_j}^{(t_2)_j} (N_{\mathrm{AB}})_i \right) \times \frac{(t_2)_j - (t_1)_j}{\sum_{i=(t_1)_j}^{(t_2)_j} T_i} - \left(\sum_{i=(t_1)_j-(t_0+\Delta t)}^{(t_1)_j-t_0} (N_{\mathrm{AB}})_i \right) \times \frac{(t_2)_j - (t_1)_j}{\sum_{(t_1)_j-(t_0+\Delta t)}^{(t_1)_j-t_0} T_i} \right] \tag{3.5}$$

where M_{A} is the number of clusters of type A normalized per area unit and luminosity unit. In the case of LETP cluster types A are dots, small blobs and curly tracks. $(N_{\mathrm{AB}})_i$ is the number of clusters of type A below the convertor B in i-th frame during the j-th collision period. This number is already corrected for the overlapping tracks (section 3.2.1). In the case of LETP, all convertors together are considered as convertor B, i.e., clusters from the whole sensor chip area are counted. L_j is the integrated luminosity during the j-th collision period, S_{B} is the area of the convertor B, T_i is the acquisition time of the i-th frame during the j-th collision period, and t_{1j}, t_{2j} is the start time and end time of the j-th collision period, respectively [5].

The first term in the big brackets in eq. (3.5) represents the sum of clusters corrected for the real detector measurement time. The second term represents the subtraction of the mean background determined from the frames between the time $(t_0 - \Delta t)$ and t_0 before the start of the j-th collision period. In most cases time t_0 was set to 30 min and Δt to 180 min. Such values of t_0 and Δt allow one to neglect frames obtained just before or after the collision period because these frames include clusters caused by photons emitted from short lived activation products (after a collision period), or signal from beam set-up (before a collision period) [5]. Typical mean background values are presented in [5].

The cluster counts $(M_{\mathrm{A}})_j$ for each cluster type A were summed to provide the measured LETP cluster count M_j for the j-th collision period. The mean value $\langle M \rangle$ and its uncertainty were calculated from cluster counts $(M_{\mathrm{A}})_j$.

2022 JINST 17 P01027

3.4.3 Comparison of measurement and simulation

Table 9 and figures 13–15 show the comparison between measurement and simulation for LETP cluster counts per unit integrated luminosity. Uncertainties are statistical only. Measured and simulated LETP cluster counts generally agree within a factor of two. In most cases, the FLUGG and GCALOR simulations give LETP cluster counts 0–40% and 20–50% lower, respectively, except for MPX07 and MPX11 where both simulations give approximately 70% higher value than measurement. As already expressed in section 3.3.3 the discrepancy for MPX11 is not so important for the overall result of the comparison because MPX11 is located on the cavern wall far from the beam line (see figure 2) where the models, especially GCALOR model, are not defined in detail. Again, there is a discrepancy between the measurements in symmetrical detectors MPX02 and MPX13, reaching approximately 40%. The possible explanation is presented in section 3.3.3.

Comparing both simulations to each other, one can notice that GCALOR gives lower LETP cluster counts than FLUGG. It can be caused by the higher electron cut off energy in GCALOR simulations (1 MeV) compared to FLUGG (0.1 MeV).

In general, the simulations provide slightly lower LETP cluster counts than the measurement but overall agreement is within 40%.

Table 9. Comparison of the average low energy transfer particles cluster count per unit integrated luminosity measured by the MPX detectors and simulated by FLUGG and GCALOR Monte Carlo codes.

Detector	MPX measurement clusters/L [cm^{-2}/nb^{-1}]	FLUGG simulation, clusters/L [cm^{-2}/nb^{-1}]	Ratio FLUGG / MPX	GCALOR simulation, clusters/L [cm^{-2}/nb^{-1}]	Ratio GCALOR / MPX
MPX01	(5.53 ± 0.33)E+04	(4.01 ± 0.01)E+04	0.72 ± 0.04	(3.58 ± 0.01)E+04	0.65 ± 0.04
MPX02	(2.29 ± 0.09)E+02	(3.22 ± 0.02)E+02	1.41 ± 0.06	(1.21 ± 0.01)E+02	0.53 ± 0.02
MPX03	(3.08 ± 0.12)E+01	(3.39 ± 0.03)E+01	1.10 ± 0.05	(1.50 ± 0.02)E+01	0.49 ± 0.02
MPX04	(1.14 ± 0.02)E+02	(4.75 ± 0.11)E+01	0.42 ± 0.01	(9.52 ± 0.10)E+01	0.84 ± 0.02
MPX05	(4.70 ± 0.17)E+01	(2.27 ± 0.04)E+01	0.48 ± 0.02	(2.23 ± 0.03)E+01	0.47 ± 0.02
MPX06	(1.97 ± 0.06)E+01	(1.17 ± 0.02)E+01	0.60 ± 0.02	(1.36 ± 0.04)E+01	0.69 ± 0.03
MPX07	(4.45 ± 0.08)E−01	(8.32 ± 0.60)E−01	1.87 ± 0.14	(7.38 ± 0.32)E−01	1.66 ± 0.08
MPX08	(1.18 ± 0.02)E+00	(1.11 ± 0.07)E+00	0.94 ± 0.06	(6.37 ± 0.31)E−01	0.54 ± 0.03
MPX09	(5.81 ± 0.17)E+00	(3.14 ± 0.21)E+00	0.54 ± 0.04	(1.71 ± 0.06)E+00	0.29 ± 0.01
MPX10	(1.03 ± 0.01)E+00	(9.35 ± 0.19)E−01	0.91 ± 0.02	(6.63 ± 0.28)E−01	0.65 ± 0.03
MPX11	(3.02 ± 0.06)E−01	(4.74 ± 0.08)E−01	1.57 ± 0.04	(5.47 ± 0.05)E−01	1.81 ± 0.04
MPX12	(3.94 ± 0.10)E+00	(2.77 ± 0.07)E+00	0.70 ± 0.03	(1.89 ± 0.02)E+00	0.48 ± 0.01
MPX13	(3.79 ± 0.10)E+02	(3.21 ± 0.02)E+02	0.85 ± 0.02	(1.21 ± 0.01)E+02	0.32 ± 0.01
MPX14	(5.40 ± 0.20)E+04	(3.97 ± 0.01)E+04	0.74 ± 0.03	(3.58 ± 0.01)E+04	0.66 ± 0.03
MPX15	(2.36 ± 0.12)E+06	(2.19 ± 0.01)E+06	0.93 ± 0.05	(2.03 ± 0.01)E+06	0.86 ± 0.04

3.4.4 Sensitivity to energy cuts

Energy cuts used to sort particles into LETP and HETP groups were derived from the experience confirmed by results of measurements performed in proton beams in HIT DKFZ in 2013 that a track left in the sensor by an 80 MeV proton is recognized by the pattern recognition algorithm as a heavy track in roughly 50% of cases only. In other cases, it is recognized as a curly track or a straight track. It means that such protons lose less energy per track length and thus behave more like minimum ionizing particles (MIPs), rather than as a heavy charged particle. Therefore, this was a starting point for the definition of the energy cuts for the sorting of particles into different particle

2022 JINST 17 P01027

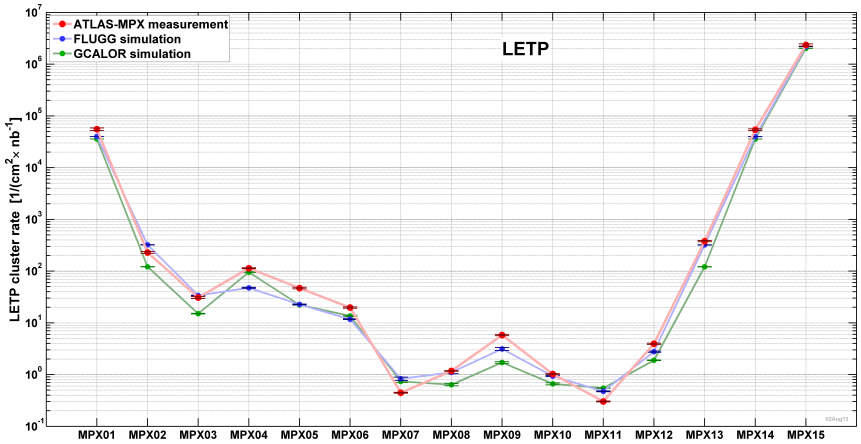

Figure 13. Comparison of low energy transfer particles cluster count per unit integrated luminosity as measured by MPX detectors (red) and simulated by FLUGG (blue) and GCALOR (green). The lines are to guide the eye.

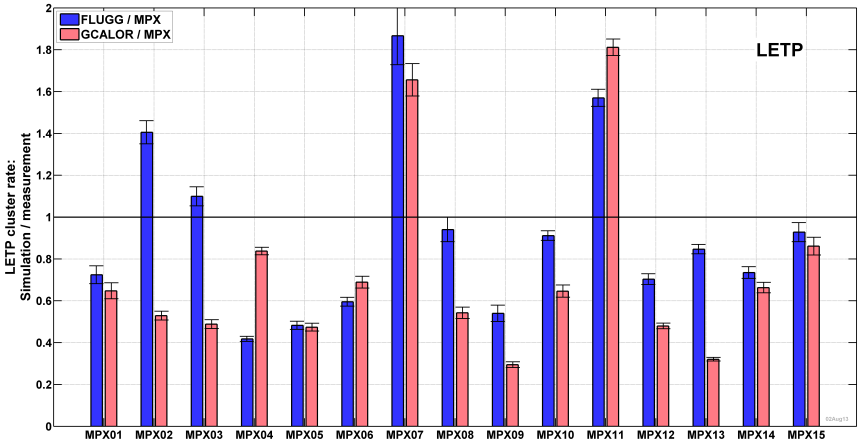

Figure 14. Ratio of simulated and measured low energy transfer particles cluster count per unit integrated luminosity. FLUGG simulation is blue, GCALOR simulation is red.

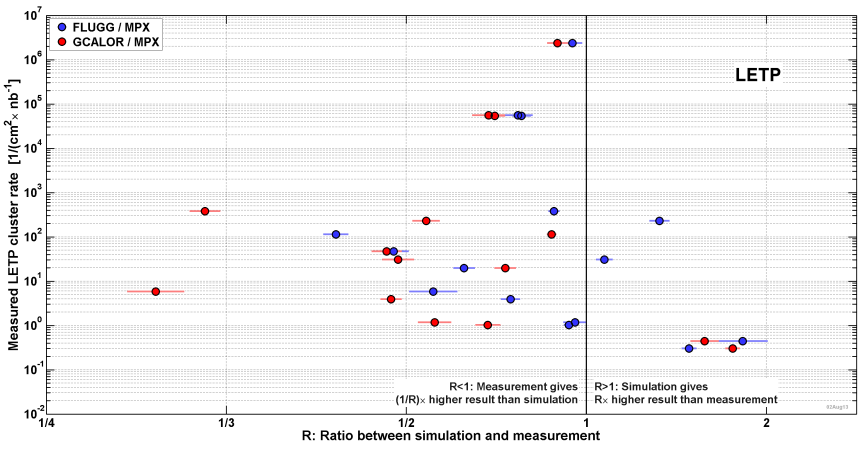

Figure 15. Ratio of simulated and measured low energy transfer particles cluster count per unit integrated luminosity. FLUGG simulation is blue, GCALOR simulation is red.

2022 JINST 17 P01027

groups. The collision stopping power, dE/dx, of 80 MeV protons in silicon is approximately 87 keV per pixel width (55 µm). At this value of the stopping power, the corresponding kinetic energies of other particles were found (see table 10). These values were set as the main energy cuts used in the comparison. In addition, four other sets of energy cuts were defined (table 10), based on the proton kinetic energy, in order to estimate the sensitivity of the simulated LETP and HETP cluster counts to the energy cuts. Nevertheless, it should be stressed that according to the above-mentioned measurements done in HIT DKFZ it is expected that the realistic border value of dE/dx between LETP and HETP clusters corresponds to the proton kinetic energy roughly between 50 and 110 MeV, depending on the track orientation with respect to the sensor.

Table 10. Main energy cuts and additional energy cuts for estimation of the sensitivity of the simulated LETP and HETP cluster counts to the energy cut values

Particles	**Main energy cut, E_{cut0}; $(dE/dx)_0$ = 87 keV/55 µm**	**E_{cut1}: (dE/dx) = 126 keV/55 µm**	**E_{cut2}: (dE/dx) = 70 keV/55 µm**	**E_{cut3}: (dE/dx) = 57 keV/55 µm**	**E_{cut4}: (dE/dx) = 47 keV/55 µm**
Protons	**80 MeV**	50 MeV	110 MeV	150 MeV	200 MeV
Muons	**9 MeV**	7.6 MeV	13 MeV	18 MeV	23 MeV
Pions	**12 MeV**	7.5 MeV	18 MeV	24 MeV	30 MeV
Charged kaons	**42 MeV**	26 MeV	60 MeV	83 MeV	105 MeV

Table 11 summarizes the sensitivity of LETP cluster counts obtained from FLUGG simulations to the energy cuts. It can be seen that the value of the simulated LETP cluster count is nearly insensitive to the selected range of energy cuts. It can be noticed in table 11 that occasionally there is no change in LETP cluster count between different E_{cut} values. This is caused by low statistics of the simulation when no particle counted into the LETP group had the kinetic energy inside the energy interval corresponding to the varied E_{cut} values.

3.5 High energy transfer particles

In this section the input simulation and measurement data used for the comparison of HETP are defined. Section 3.5.4 contains complementary discussion related to sorting particles including fast neutrons into the HETP group.

3.5.1 Simulation data

The following particles (and their anti-particles) stored in 4-vector files were filtered and counted into the simulated High Energy Transfer Particles (HETP) cluster count with the weight equal to their pre-calculated energy-angular detection efficiency (section 2.5):

- Protons with energy $E < 80$ MeV;
- Muons with energy $E < 9$ MeV;
- Charged pions with energy $E < 12$ MeV;
- Charged kaons with energy $E < 42$ MeV;
- All deuterons, tritons and alpha particles;

2022 JINST 17 P01027

Table 11. Sensitivity of the FLUGG LETP cluster count on the energy cuts values (left part of the table) and the ratio of the FLUGG and measured LETP cluster count for different energy cuts values applied for determination of FLUGG LETP cluster counts from FLUGG 4-vectors (right part of the table).

	Difference in FLUGG LETP cluster count [1]				Ratio FLUGG / MPX for LETP cluster counts				
Detector	E_{cut1}	E_{cut2}	E_{cut3}	E_{cut4}	E_{cut0}	E_{cut1}	E_{cut2}	E_{cut3}	E_{cut4}
MPX01	0.7%	−0.7%	−1.5%	−2.4%	**0.72 ± 0.04**	0.73 ± 0.04	0.72 ± 0.04	0.71 ± 0.04	0.71 ± 0.04
MPX02	0.5%	−0.6%	−1.2%	−1.9%	**1.41 ± 0.06**	1.41 ± 0.06	1.40 ± 0.05	1.39 ± 0.05	1.38 ± 0.05
MPX03	0.3%	−0.3%	−0.5%	−0.7%	**1.10 ± 0.05**	1.10 ± 0.05	1.10 ± 0.05	1.09 ± 0.05	1.09 ± 0.05
MPX04	1.3%	−1.5%	−2.5%	−2.6%	**0.42 ± 0.01**	0.42 ± 0.01	0.41 ± 0.01	0.41 ± 0.01	0.41 ± 0.01
MPX05	0.7%	−0.3%	−0.9%	−1.0%	**0.48 ± 0.02**	0.49 ± 0.02	0.48 ± 0.02	0.48 ± 0.02	0.48 ± 0.02
MPX06	0.1%	−0.7%	−1.2%	−1.5%	**0.60 ± 0.02**	0.60 ± 0.02	0.59 ± 0.02	0.59 ± 0.02	0.59 ± 0.02
MPX07	0.0%	0.0%	0.0%	0.0%	**1.87 ± 0.14**	1.87 ± 0.14	1.87 ± 0.14	1.87 ± 0.14	1.87 ± 0.14
MPX08	1.2%	0.0%	0.0%	0.0%	**0.94 ± 0.06**	0.95 ± 0.06	0.94 ± 0.06	0.94 ± 0.06	0.94 ± 0.06
MPX09	0.0%	0.0%	0.0%	0.0%	**0.54 ± 0.04**	0.54 ± 0.04	0.54 ± 0.04	0.54 ± 0.04	0.54 ± 0.04
MPX10	0.0%	0.0%	0.0%	0.0%	**0.91 ± 0.02**	0.91 ± 0.02	0.91 ± 0.02	0.91 ± 0.02	0.91 ± 0.02
MPX11	0.0%	0.0%	0.0%	0.0%	**1.57 ± 0.04**	1.57 ± 0.04	1.57 ± 0.04	1.57 ± 0.04	1.57 ± 0.04
MPX12	0.3%	−0.6%	−0.6%	−0.9%	**0.70 ± 0.03**	0.71 ± 0.03	0.70 ± 0.02	0.70 ± 0.02	0.70 ± 0.02
MPX13	0.5%	−0.6%	−1.1%	−1.7%	**0.85 ± 0.02**	0.85 ± 0.02	0.84 ± 0.02	0.84 ± 0.02	0.83 ± 0.02
MPX14	0.6%	−0.7%	−1.6%	−2.4%	**0.74 ± 0.03**	0.74 ± 0.03	0.73 ± 0.03	0.72 ± 0.03	0.72 ± 0.03
MPX15	0.1%	−0.1%	−0.2%	−0.3%	**0.93 ± 0.05**	0.93 ± 0.05	0.93 ± 0.05	0.93 ± 0.05	0.93 ± 0.05

[1] Calculated as $(L_x\text{-}L_0)/L_0$ where L_x is the LETP cluster count for different energy cuts and L_0 is the LETP cluster count calculated for main energy cuts. All values of E_{cut} are defined in table 10.

- Fast neutrons (a fast neutron causes an HETP signal if the energy deposition in the sensor chip is higher than 230 keV, i.e., mainly through interactions with silicon nuclei in the sensor chip by elastic, inelastic scattering and nuclear reactions ((n,p), (n,α), spallation, deeply inelastic processes, etc.) and through protons recoiled by fast neutrons in the polyethylene conversion layer).

The relative contribution of different particle types counted into the simulated HETP cluster count in every MPX detector is shown in table 12. The uncertainty is not presented. However, it can be roughly estimated from the number of particles counted into the HETP cluster count summarized in tables 2 and 3. In general, both simulations are consistent. A slight disagreement was observed in MPX05, MPX12 and MPX15.

3.5.2 Measurement data

High energy transfer particles are those which create a thick track in the MPX detector, i.e., particles with the energy loss in silicon higher than approximately 87 keV per 55 µm. Such particles are of the most interest for an estimation of the radiation damage of electronics. The HETP cluster count was calculated independently for each collision period using eq. (3.5). The cluster types counted included heavy blobs and heavy tracks in the whole sensor except for those in the ^{6}LiF. Cluster counts below different converter layers (except for ^{6}LiF) were not treated independently because in the ATLAS radiation field the HETP response below different converters differs within few tenths of a percent only. Cluster counts of both cluster types were subsequently summed and the resulting mean value of the measured HETP cluster count and its uncertainty were calculated.

2022 JINST 17 P01027

Table 12. Relative contribution of particles into the total simulated HETP cluster count.

	FLUGG simulation					GCALOR simulation				
	Neutrons	**Muons**	**Pions**	**Protons**	**Kaons**	**Neutrons**	**Muons**	**Pions**	**Protons**	**Kaons**
MPX01	14.8%	4.5%	5.1%	75.4%	0.3%	16.0%	2.6%	3.7%	77.4%	0.3%
MPX02	55.4%	0.0%	1.3%	43.3%	0.0%	58.0%	0.6%	2.1%	39.3%	0.0%
MPX03	76.3%	0.0%	1.0%	22.7%	0.0%	79.1%	0.0%	0.3%	20.6%	0.0%
MPX04	67.6%	0.0%	0.0%	32.4%	0.0%	65.8%	0.0%	0.0%	34.2%	0.0%
MPX05	65.7%	0.0%	0.0%	34.3%	0.0%	86.5%	0.0%	0.0%	13.5%	0.0%
MPX06	70.1%	0.0%	0.0%	29.9%	0.0%	67.0%	0.0%	0.0%	33.0%	0.0%
MPX07	100.0%	0.0%	0.0%	0.0%	0.0%	86.3%	0.0%	0.0%	13.7%	0.0%
MPX08	39.4%	0.0%	0.0%	60.6%	0.0%	46.0%	0.0%	0.0%	54.0%	0.0%
MPX09	66.5%	0.0%	0.0%	33.5%	0.0%	73.8%	0.0%	0.0%	26.2%	0.0%
MPX10	100.0%	0.0%	0.0%	0.0%	0.0%	100.0%	0.0%	0.0%	0.0%	0.0%
MPX11	99.6%	0.0%	0.0%	0.4%	0.0%	100.0%	0.0%	0.0%	0.0%	0.0%
MPX12	37.9%	0.2%	0.0%	61.9%	0.0%	81.0%	0.0%	0.0%	19.0%	0.0%
MPX13	55.6%	0.3%	0.7%	42.8%	0.7%	58.0%	0.6%	2.1%	39.3%	0.0%
MPX14	15.4%	4.7%	4.3%	75.5%	0.2%	16.0%	2.6%	3.7%	77.4%	0.3%
MPX15	32.3%	0.2%	1.8%	65.6%	0.1%	21.6%	0.0%	3.3%	75.1%	0.0%

3.5.3 Comparison of measurement and simulation

Table 13 and figures 16–18 show the comparison between measurement and simulation for HETP cluster counts per unit integrated luminosity. Measured and simulated HETP cluster counts generally agree within a factor of 2. In most cases, the simulations give cluster counts higher than the measurements. A significant discrepancy was obtained for MPX07 in GCALOR simulation only, but this is caused by the oversimplification of the ATLAS cavern model. As mentioned earlier, again

Table 13. Comparison of the average high energy transfer particles cluster count per unit integral luminosity measured by the MPX detectors and simulated by FLUGG and GCALOR Monte Carlo codes

Detector	**MPX measurement clusters/L [cm^{-2}/nb^{-1}]**	**FLUGG simulation, clusters/L [cm^{-2}/nb^{-1}]**	**Ratio FLUGG/MPX**	**GCALOR simulation, clusters/L [cm^{-2}/nb^{-1}]**	**Ratio GCALOR/MPX**
MPX01	(5.72 ± 0.40)E+02	(5.74 ± 0.06)E+02	1.00 ± 0.07	(6.05 ± 0.06)E+02	1.06 ± 0.08
MPX02	(3.32 ± 0.14)E+00	(7.98 ± 0.18)E+00	2.41 ± 0.12	(3.52 ± 0.12)E+00	1.06 ± 0.06
MPX03	(4.87 ± 0.24)E−01	(9.41 ± 0.29)E−01	1.93 ± 0.11	(5.54 ± 0.20)E−01	1.14 ± 0.07
MPX04	(1.69 ± 0.04)E+00	(2.88 ± 0.15)E+00	1.70 ± 0.10	(2.87 ± 0.14)E+00	1.70 ± 0.09
MPX05	(4.86 ± 0.22)E−01	(8.27 ± 0.59)E−01	1.70 ± 0.15	(3.27 ± 0.12)E−01	0.67 ± 0.04
MPX06	(2.08 ± 0.08)E−01	(4.01 ± 0.29)E−01	1.93 ± 0.16	(2.84 ± 0.21)E−01	1.37 ± 0.12
MPX07	(4.04 ± 0.30)E−03	(3.27 ± 0.16)E−03	0.81 ± 0.07	(4.45 ± 0.29)E−02	11.04 ± 1.08
MPX08	(1.09 ± 0.06)E−02	(2.27 ± 0.97)E−02	2.08 ± 0.90	(1.35 ± 0.73)E−02	1.24 ± 0.67
MPX09	(8.73 ± 0.35)E−02	(8.99 ± 1.52)E−02	1.03 ± 0.18	(1.67 ± 0.17)E−01	1.91 ± 0.21
MPX10	(1.07 ± 0.06)E−02	(1.44 ± 0.06)E−02	1.35 ± 0.09	(2.51 ± 0.08)E−02	2.35 ± 0.15
MPX11	(6.24 ± 0.38)E−03	(6.86 ± 0.23)E−03	1.10 ± 0.08	(1.03 ± 0.02)E−02	1.65 ± 0.10
MPX12	(5.16 ± 0.19)E−02	(1.83 ± 0.14)E−01	3.55 ± 0.29	(7.29 ± 0.27)E−02	1.41 ± 0.07
MPX13	(5.32 ± 0.18)E+00	(7.94 ± 0.18)E+00	1.49 ± 0.06	(3.52 ± 0.12)E+00	0.66 ± 0.03
MPX14	(5.75 ± 0.23)E+02	(5.48 ± 0.05)E+02	0.95 ± 0.04	(6.05 ± 0.06)E+02	1.05 ± 0.04
MPX15	(9.23 ± 0.49)E+03	(4.72 ± 0.02)E+03	0.51 ± 0.03	(7.02 ± 0.32)E+03	0.76 ± 0.05

2022 JINST 17 P01027

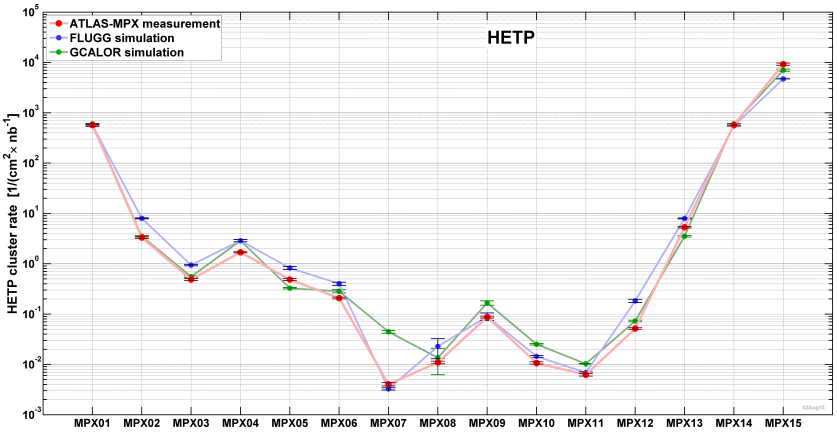

Figure 16. Comparison of high energy transfer particles cluster count per unit integrated luminosity as measured by MPX detectors (red) and simulated by FLUGG (blue) and GCALOR (green). The lines are to guide the eye.

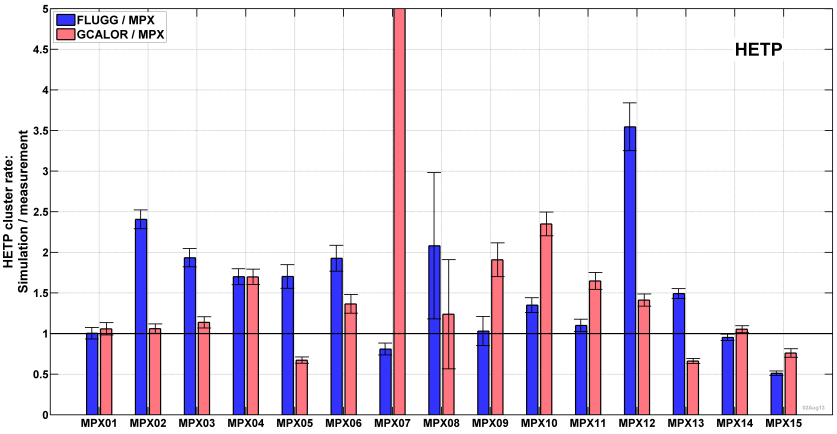

Figure 17. Ratio of simulated and measured high energy transfer particles cluster count per unit integrated luminosity. FLUGG simulation is blue, GCALOR simulation is red. Note that GCALOR/MPX07 ratio (11.04±1.08, see table 13) goes out of the scale.

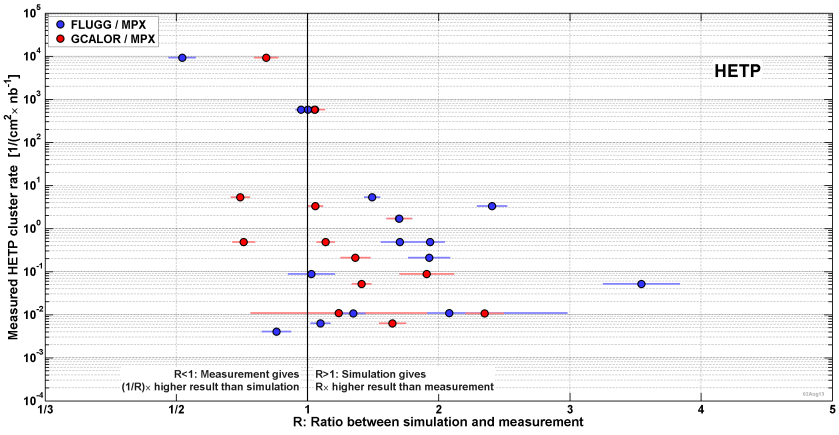

Figure 18. Ratio of simulated and measured high energy transfer particles cluster count per unit integrated luminosity. FLUGG simulation is blue, GCALOR simulation is red.

2022 JINST 17 P01027

there is a discrepancy between the measurements in symmetrical detectors MPX02 and MPX13, reaching approximately 40%. The possible explanation is presented in section 3.3.3.

It can be concluded that the overall agreement between the HETP cluster count measurement and both simulations is very good.

3.5.4 Sensitivity to energy cuts

The same sensitivity study as for the LETP cluster counts (see section 3.4.4) was done for the HETP cluster counts as well. Table 14 summarizes the sensitivity of the HETP cluster counts calculated from FLUGG 4-vectors as a function of the selected energy cuts defined in table 10 in section 3.4.4.

Table 14. Sensitivity of the FLUGG HETP cluster count on the energy cuts values (left part of the table) and the ratio of the FLUGG and measured HETP cluster count for different energy cuts values applied for determination of FLUGG HETP cluster counts from FLUGG 4-vectors (right part of the table).

	Difference in FLUGG HETP cluster count [(1)]				**Ratio FLUGG / MPX for HETP cluster counts**				
Detector	E_{cut1}	E_{cut2}	E_{cut3}	E_{cut4}	E_{cut0}	E_{cut1}	E_{cut2}	E_{cut3}	E_{cut4}
MPX01	−47.0%	51.1%	110.3%	171.8%	**1.00 ± 0.07**	0.53 ± 0.04	1.52 ± 0.11	2.11 ± 0.15	2.73 ± 0.19
MPX02	−23.0%	28.5%	57.1%	90.1%	**2.41 ± 0.12**	1.85 ± 0.09	3.09 ± 0.15	3.78 ± 0.19	4.57 ± 0.23
MPX03	−14.3%	14.5%	22.2%	33.0%	**1.93 ± 0.11**	1.66 ± 0.09	2.22 ± 0.14	2.36 ± 0.15	2.57 ± 0.17
MPX04	−23.7%	25.3%	42.9%	45.4%	**1.70 ± 0.10**	1.30 ± 0.05	2.13 ± 0.14	2.43 ± 0.18	2.47 ± 0.18
MPX05	−20.9%	9.1%	27.7%	32.9%	**1.70 ± 0.15**	1.35 ± 0.08	1.86 ± 0.16	2.18 ± 0.20	2.26 ± 0.21
MPX06	−8.1%	19.9%	37.0%	46.7%	**1.93 ± 0.16**	1.77 ± 0.15	2.31 ± 0.22	2.64 ± 0.29	2.83 ± 0.32
MPX07	0.0%	165.3%	165.3%	165.3%	**0.81 ± 0.07**	0.81 ± 0.07	2.15 ± 1.35	2.15 ± 1.35	2.15 ± 1.35
MPX08	−60.6%	0.0%	0.0%	0.0%	**2.08 ± 0.90**	0.82 ± 0.06	2.08 ± 0.90	2.08 ± 0.90	2.08 ± 0.90
MPX09	−5.0%	0.0%	0.0%	0.0%	**1.03 ± 0.18**	0.98 ± 0.18	1.03 ± 0.18	1.03 ± 0.18	1.03 ± 0.18
MPX10	0.0%	41.2%	41.2%	41.2%	**1.35 ± 0.09**	1.35 ± 0.09	1.91 ± 0.41	1.91 ± 0.41	1.91 ± 0.41
MPX11	0.0%	12.1%	12.1%	12.1%	**1.10 ± 0.08**	1.10 ± 0.08	1.23 ± 0.12	1.23 ± 0.12	1.23 ± 0.12
MPX12	−33.0%	11.9%	14.3%	20.1%	**3.55 ± 0.29**	2.38 ± 0.20	3.97 ± 0.45	4.05 ± 0.45	4.26 ± 0.47
MPX13	−24.4%	26.2%	53.4%	82.1%	**1.49 ± 0.06**	1.13 ± 0.04	1.88 ± 0.08	2.29 ± 0.10	2.72 ± 0.12
MPX14	−44.2%	52.6%	116.6%	181.7%	**0.95 ± 0.04**	0.53 ± 0.02	1.45 ± 0.06	2.06 ± 0.08	2.68 ± 0.11
MPX15	−39.1%	43.6%	95.4%	143.8%	**0.51 ± 0.03**	0.31 ± 0.02	0.73 ± 0.04	1.00 ± 0.05	1.25 ± 0.07

[(1)] Calculated as $(H_x - H_0)/H_0$ where H_x is the HETP cluster count for modified energy cuts and H_0 is the HETP cluster count calculated for main energy cuts. All values of E_{cut} are defined in table 10.

There is a significant difference in the simulated HETP cluster count when the $\mathrm{d}E/\mathrm{d}x$ energy cuts are varied. However, the highest (E_{cut1}) and lowest (E_{cut4}) $\mathrm{d}E/\mathrm{d}x$ values used in this study represent the limits inside which the effective border between the LETP and HETP group lies. In fact, a complementary investigation of the response to energetic protons performed in proton beams in HIT DKFZ showed, that the realistic border of $\mathrm{d}E/\mathrm{d}x$ value between the recognition of LETP and HETP clusters corresponds to the proton kinetic energy roughly between 50 and 110 MeV [28, 29], i.e., between the values of E_{cut1} and E_{cut2}. Then, the values in table 14 corresponding to E_{cut1} and E_{cut2} represent the systematic uncertainty on the interpretation of HETP cluster count observation for the comparison with Monte Carlo simulations. In other words, the systematic uncertainty on the HETP cluster counts comparison is 50% for MPX01 and 14, 40% for MPX15, 30% for MPX02 and 13, and 20% for MPX03-12. It can be also seen from table 14 that occasionally there is no change in the simulated HETP cluster count for different E_{cut} values. This is caused by low statistics of the simulation when no particle counted into the HETP group had the kinetic energy inside the energy interval corresponding to the varied E_{cut} values. By contrast, occasionally there is a huge change in the simulated HETP cluster count between different E_{cut} values. This occurs when only one or very

2022 JINST 17 P01027

few particles counted into the HETP group had the kinetic energy inside the given energy interval. The ratio and its uncertainty then change accordingly.

4 Conclusions

Results of measurements performed with MPX detectors during the LHC operation period in 2010 and 2011 have been compared with Monte Carlo simulation results from the FLUGG and GCALOR codes. For the purpose of this comparison, data obtained with the MPX detectors operated in tracking mode were considered. In their tracking mode of operation, the MPX detectors set at low threshold are able to distinguish particle groups based on the recognition of a track pattern left by the particles in the sensor. This required the acquisition time of MPX to be set short enough to avoid high track overlap and allowing one to distinguish the tracks created by the individual particle interactions. For the purpose of the comparison of MPX measurements with simulation, it was found convenient to use the following particle categories with different types of clusters assigned to each particle group: with low energy transfer (LETP) — electrons, gamma rays, X-rays; particles with high energy transfer (HETP) — alphas, protons, heavier ions, fast neutrons, and thermal neutrons. The measured data used for the comparison were obtained between the 15 May 2011 and the 28 October 2011, MPX01, 14 and 15 excepted as these detectors were set in other measurement mode unsuitable for the comparison described in this article. Results for MPX01, 14 and 15 were obtained from measurements performed between 15 May 2010 and 30 August 2010. Luminosity data used to normalize the cluster counts and fluences were obtained from the ATLAS luminosity database. The cluster counts and fluences were calculated independently for each collision period and then used to calculate the mean value, which was used in the comparison.

The FLUGG and GCALOR simulation data consisted of 4-vectors for all particles entering the scoring volumes. Analysis of FLUGG and GCALOR 4-vectors made possible the estimate of values of simulated LETP and HETP cluster counts and thermal neutron fluences, which could be compared to measurements. Comparison between measured thermal neutron fluence per unit integrated luminosity of all MPX detectors with simulated fluences generally agrees within a factor of two (with the measured values generally lower than simulated ones). The LETP cluster count per unit integrated luminosity comparison shows systematically higher measured values, on average about 25% and 40% higher for FLUGG and GCALOR, respectively. Comparison between measured and simulated HETP cluster counts per unit integrated luminosity generally agrees within a factor of 2 with measured values systematically lower than simulated values. The possible effect of the value of selected energy cuts on this comparison was considered. It was found that there were no significant changes to the simulated LETP cluster count. However, the electron energy cut in GCALOR simulation may have an influence on the value of the LETP cluster count calculated from GCALOR 4-vector files. Overall, the value of the simulated GCALOR and FLUGG LETP cluster count is found nearly insensitive to the selected value of energy cuts. On the other hand, the energy cut influenced the value of the HETP cluster counts calculated from 4-vector files.

The study shows that the agreement between measured and simulated data is satisfactory in most cases. Measurements of the HETP cluster counts are of the highest importance for estimating the safety factors to be used in the future for the determination of the viability of the ATLAS electronics

2022 JINST 17 P01027

exposed to growing fluences and doses of hadrons, neutrons and photons, in particular in view of future beam energy and luminosity upgrades.

The results of this work devoted to a comprehensive comparison of measurement and simulation of the ATLAS cavern radiation background were followed by partial measurements carried out with networks of the novel Timepix (TPX) [27] detectors. The first results from the ATLAS-TPX network obtained during ATLAS Run-2 have already been published to a limited extent in [30] and [31]. The measured results of thermal neutron fluence distributions in the ATLAS environment according to [30] are quite consistent with the results obtained with the ATLAS-MPX network presented in this article.

Acknowledgments

The authors greatly appreciate the cooperation and valuable advices they received from ATLAS colleagues Marzio Nessi, Beniamino di Girolamo, Ludovico Pontecorvo and Francesco Lanni.

This work was supported by Ministry of Education, Youth and Sports of the Czech Republic in frame of the projects LA08032 and LG13009 and from European Regional Development Fund-Projects No. CZ.02.1.01/0.0/0.0/16_019/0000766 and No. CZ.02.1.01/0.0/0.0/16_013/0001785.

The authors' partnership with the Medipix2 collaboration significantly also contributed to the implementation of ATLAS-MPX network.

References

[1] Y. Fisyak, O. Tsai, F. Videbæk and Z. Xu, *Thermal neutron flux measurements in the STAR experimental hall*, *Nucl. Instrum. Meth. A* **756** (2014) 68 [arXiv:1310.2495].

[2] D.E. Groom, *Radiation Levels in SSC Detectors*, *Nucl. Instrum. Meth. A* **279** (1989) 1.

[3] M.V. Diwan et al., *Radiation environment and shielding for a high luminosity collider detector*, Tech. Rep., BNL-52492 Formal Report, SSCL-SR-1223 (1995).

[4] S. Baranov, M. Bosman, I. Dawson, V. Hedberg, A. Nisati and M. Shupe, *Estimation of Radiation Background, Impact on Detectors, Activation and Shielding Optimization in ATLAS*, Tech. Rep., ATL-GEN-2005-001, ATL-COM-GEN-2005-001, CERN-ATL-GEN-2005-001, CERN, Geneva (2005).

[5] M. Campbell, E. Heijne, C. Leroy, J.-P. Martin, G. Mornacchi, M. Nessi et al., *Analysis of the Radiation Field in ATLAS Using 2008 2011 Data from the ATLAS-MPX Network*, Tech. Rep., ATL-GEN-PUB-2013-001, CERN, Geneva (2013).

[6] CERN Medipix2 collaboration, http://www.cern.ch/medipix.

[7] M. Campbell, E. Heijne, C. Leroy, M. Nessi, S. Pospisil, J. Solc et al., *Induced radioactivity in ATLAS cavern measured by MPX detector network*, 2019 *JINST* **14** P03010.

[8] M. Campbell, E. Heijne, C. Leroy, M. Nessi, S. Pospisil, J. Solc et al., *Penetration of ionizing radiation from ATLAS cavern into USA15 measured by MPX detectors*, 2019 *JINST* **14** P02020.

[9] T. Lanni, *Report of the Radiation Estimate Task-Force*, CERN (2013), https://indico.cern.ch/event/280107/contributions/633342/attachments/513266/708323/FL_RETF_Report.pdf.

[10] A. Breskin and R. Voss, *The CERN Large Hadron Collider: Accelerator and Experiments Volume 1: LHC machine, ALICE and ATLAS*, first edition, CERN, Geneva (2008) [ISBN: 978-92-9083-337-6].

2022 JINST 17 P01027

[11] ATLAS collaboration, *ATLAS technical coordination: Technical Design Report*, Tech. Rep., CERN-LHCC-99-001, ATLAS-TDR-13, ATLAS, CERN, Geneva (1999).

[12] D.B. Pelowitz et al., 2011. "MCNPX™ 2.7.E extensions", Tech. Rep., LA-UR-11-01502.

[13] J. Bougher, D. Brown, T. Koi, P. Sherwood, D. Wright and Ch. Young, *A FLUGG-based Cavern background Simulation Application*, Tech. Rep., ATL-COM-SOFT-2011-032, CERN, Geneva (2011).

[14] FLUGG, http://www.fluka.org/content/tools/flugg/index.html.

[15] Shielding Project web page, http://atlas.web.cern.ch/Atlas/GROUPS/Shielding/shielding.htm.

[16] G. Aielli, *Cavern background measurement with the ATLAS RPC system*, Tech. Rep., ATL-MUON-PROC-2012-005, CERN, Geneva (2012).

[17] T. Koi, I. Mandić and Ch. Young, *Comparison of FLUGG simulations of fluence and dose in the ATLAS inner detector with RADMON measurements*, Tech. Rep., ATL-COM-GEN-2013-004, 2013.

[18] Ch. Young, *Dose in Calorimeter Regions*, presented at the *Radiation Estimation Task Force meeting*, CERN, 26 April 2013.

[19] R. Engel, *PHOJET Manual*, http://physik.uni-leipzig.de/~eng/phojet.html.

[20] C. Zeinitz, *GCALOR Simulation Package*, http://www.atlas.uni-wuppertal.de/zeitnitz/gcalor.

[21] M. Shupe, private communication, 2010.

[22] ICRP, *Conversion Coefficients for use in Radiological Protection against External Radiation*, *ICRP Publication 74*, *Ann. ICRP* **26** (3–4), 1996.

[23] TOTEM collaboration, *First measurement of the total proton-proton cross section at the LHC energy of* $\sqrt{s} = 7$ *TeV*, *EPL* **96** (2011) 21002. 11 p [arXiv:1110.1395] [CERN-PH-EP-2011-158].

[24] ATLAS collaboration, *Improved luminosity determination in pp collisions at sqrt(s) = 7 TeV using the ATLAS detector at the LHC*, *Eur. Phys. J. C* **73** (2013) 2518 [arXiv:1302.4393].

[25] D.A. Brown et al., *ENDF/B-VIII.0: The 8th Major Release of the Nuclear Reaction Data Library with CIELO-project Cross Sections, New Standards and Thermal Scattering Data*, *Nucl. Data Sheets* **148** (2018) 1.

[26] C. Leroy, S. Pospisil, M. Suk and Z. Vykydal, *Proposal to Measure Radiation Field Characteristics, Luminosity and Induced Radioactivity in ATLAS with TIMEPIX Devices*, ATL-COM-GEN-2014-005.

[27] X. Llopart, R. Ballabriga, M. Campbell, L. Tlustos and W. Wong, *Timepix, a 65k programmable pixel readout chip for arrival time, energy and/or photon counting measurements*, *Nucl. Instrum. Meth. A* **581** (2007) 485 [*Erratum ibid.* **585** (2008) 106]

[28] L. Opalka et al., *3D measurement of the radiation distribution in a water phantom in a hadron therapy beam*, 2012 *JINST* **7** C01085.

[29] L. Opalka et al., *Linear energy transfer and track pattern recognition of secondary radiation generated in hadron therapy beam in a PMMA target*, 2013 *JINST* **8** C02047.

[30] B. Bergmann, I. Caicedo, C. Leroy, S. Pospisil and Z. Vykydal, *ATLAS-TPX: a two-layer pixel detector setup for neutron detection and radiation field characterization*, 2016 *JINST* **11** P10002.

[31] B. Bergmann, T. Billoud, C. Leroy and S. Pospisil, *Characterization of the Radiation Field in the ATLAS Experiment With Timepix Detectors*, *IEEE Trans. Nucl. Sci.* **66** (2019) 1861.

2022 JINST 17 P01027